

Simulating Open Quantum System Dynamics on NISQ Computers with Generalized Quantum Master Equations

Yuchen Wang,[†] Ellen Mulvihill,[‡] Zixuan Hu,[†] Ningyi Lyu,[‡] Saurabh Shivpuje,[†]
Yudan Liu,[¶] Micheline B. Soley,^{‡,§} Eitan Geva,^{*,¶} Victor S. Batista,^{*,‡} and Sabre
Kais^{*,†}

[†]*Department of Chemistry, Department of Physics and Purdue Quantum Science and
Engineering Institute, Purdue University, West Lafayette, Indiana 47907, USA*

[‡]*Department of Chemistry, Yale Quantum Institute, Yale University, New Haven, CT
06511, USA*

[¶]*Department of Chemistry, University of Michigan, Ann Arbor, MI 48109, USA*

[§]*Department of Chemistry, Department of Physics, University of Wisconsin-Madison,
Madison, WI 53706, USA*

E-mail: eitan@umich.edu; victor.batista@yale.edu; kais@purdue.edu

Abstract

We present a quantum algorithm based on the Generalized Quantum Master Equation (GQME) approach to simulate open quantum system dynamics on noisy intermediate-scale quantum (NISQ) computers. This approach overcomes the limitations of the Lindblad equation, which assumes weak system-bath coupling and Markovity, by providing a rigorous derivation of the equations of motion for any subset of elements of the reduced density matrix. The memory kernel resulting from the effect of the remaining

degrees of freedom is used as input to calculate the corresponding non-unitary propagator. We demonstrate how the Sz.-Nagy dilation theorem can be employed to transform the non-unitary propagator into a unitary one in a higher-dimensional Hilbert space, which can then be implemented on quantum circuits of NISQ computers. We validate our quantum algorithm as applied to the spin-boson benchmark model by analyzing the impact of the quantum circuit depth on the accuracy of the results when the subset is limited to the diagonal elements of the reduced density matrix. Our findings demonstrate that our approach yields reliable results on NISQ IBM computers.

1 Introduction

Simulations of open quantum systems have become essential for studying the dynamics of quantum systems in the condensed phase, allowing for the inclusion of dissipative effects from the environment which are critical for accurate simulations. These powerful computational tools have enabled a wide range of studies, from chemical and physical processes to excited state lifetimes, spectral diffusion and line-broadening, across multiple fields of research, including physical chemistry, molecular physics, condensed-phase physics, nanoscience, molecular electronics, quantum optics, nonequilibrium statistical mechanics, spectroscopy and quantum information science.¹⁻³⁰ Examples of open quantum system dynamics include energy and charge transfer, dephasing, vibrational relaxation, nonadiabatic dynamics and photochemistry (see Fig. 1). By harnessing the power of open quantum system simulations, we can bridge the gap between theory and experiment, providing insight into various complex phenomena in a variety of light-induced physical and chemical processes, including photoinduced processes such as energy and charge transfer, vibronic relaxation, dephasing, and nonadiabatic dynamics.^{22,23,28,31-49}

Recent advances in quantum computing have enabled the development of numerous algorithms for electronic structure calculations,⁵⁰⁻⁵³ and simulations of quantum dynamics of closed quantum systems.⁵⁴⁻⁵⁷ However, relatively few studies have explored the simulation

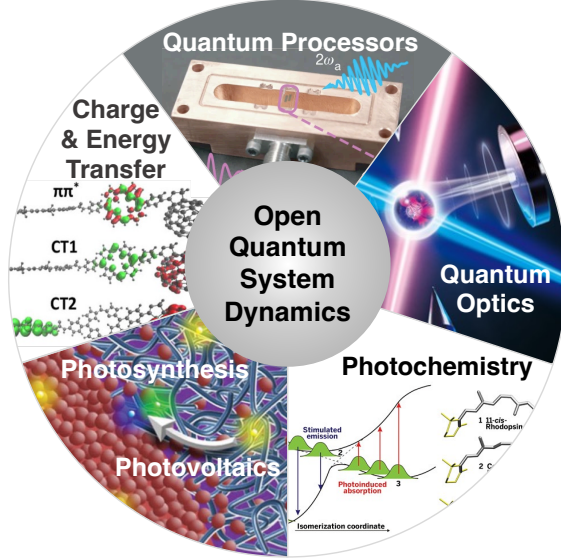


Figure 1: The simulation of open quantum system dynamics is central to many science and engineering disciplines (a few examples are showcased in the figure).

of open quantum system dynamics.^{58–67} These studies have been mostly based on Lindblad-type quantum master equations (QMEs) which ensure complete positivity and conservation of probability but rely on the Markov and Born approximations in the system-bath weak coupling limit.⁹ With the aim of developing a more general approach, here we introduce a quantum algorithm based on the Generalized Quantum Master Equation (GQME), which corresponds to the formally exact equation of motion (EoM) for an open quantum system.

A major challenge facing the quantum simulation of open quantum system dynamics is the fact that the time evolution operators are non-unitary whereas quantum gates are unitary. To this end, we have previously developed a quantum algorithm for open quantum dynamics based on the Sz.-Nagy unitary dilation theorem, which converts non-unitary operators into unitary operators in an extended Hilbert space. This algorithm was originally applied to simulating a Markovian two-level model on IBM quantum computers.⁶⁸ Later, the same method was applied to simulating the non-Markovian Jaynes-Cummings model on IBM quantum computers.⁶⁹ In a recent work, the same Lindblad-QME-based quantum algorithm was applied to simulate the dynamics of the Fenna-Matthews-Olson complex, which includes five quantum states and seven elementary physical processes.⁷⁰ Thus far, this quan-

tum algorithm has been used to simulate the dynamics of open quantum systems described by the operator sum representation or Lindblad-type QMEs.

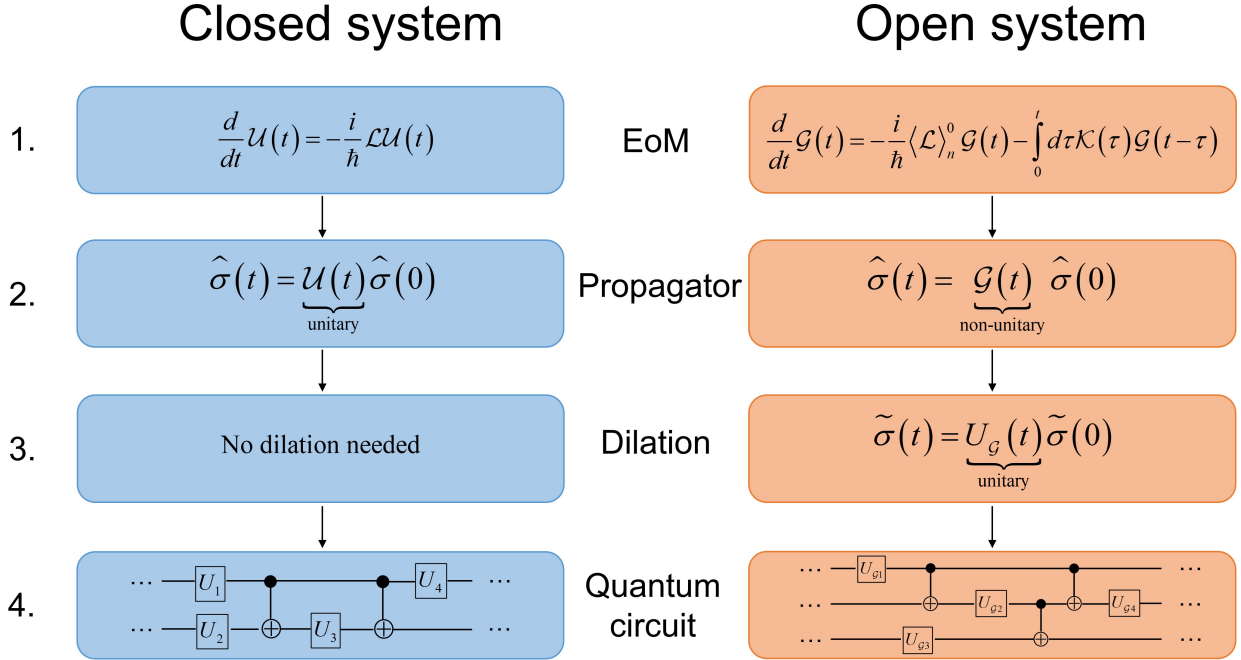


Figure 2: A comparison of the workflows for simulating the dynamics of a closed quantum system governed by the quantum Liouville equation vs. an open quantum system governed by the GQME. 1. The EoM is established; 2. the time evolution superoperator is generated from the EoM; 3. A unitary dilation is required in order to convert the GQME-based non-unitary time evolution superoperator into a unitary superoperator in an extended Hilbert space; 4. Translation of the unitary matrix into a quantum gate sequence.

However, these approaches are not entirely general: the Lindblad QME used in Ref. 70 relies on several restrictive approximations, including Markovian dynamics, and the ensemble of Lindbladian trajectories method in Ref. 69, while capable of describing non-Markovian dynamics, involves user selection of *ad-hoc* system-bath parameters, therefore limiting the range of applications. Furthermore, while the operator sum representation of open quantum system dynamics is general, it requires knowledge of the Kraus operators, which to the best of our knowledge are only known in closed form for systems whose dynamics can be described by Lindblad-type QMEs.

Extending the range of quantum simulation of open quantum systems therefore calls

for formulating the dynamics within a less restrictive theoretical framework. The GQME formalism introduced by Nakajima⁷¹ and Zwanzig⁷² represents such a general framework since the GQME corresponds to the formally exact EoM of the open quantum system, as opposed to the Lindblad-type QMEs which correspond to approximate EoMs of the open quantum system.

A comparison of the workflows for simulating the dynamics of a closed quantum system governed by the quantum Liouville equation vs. an open quantum system governed by the GQME is shown in Fig. 2. The derivation of the GQME involves projecting out the bath degrees of freedom (DOF) to obtain the EoM of the system’s reduced density matrix, or a subset of its elements. Within this EoM, which is referred to as the GQME, the memory kernel superoperator, $\mathcal{K}(\tau)$, accounts for the main impact of the bath on the system’s dynamics. Thus, the GQME replaces the Liouville equation as the formally exact EoM of the system when we transition from a closed quantum system to an open quantum system, with the memory kernel playing a similar role in the open system to that of the Hamiltonian or Liouvillian in the closed system.

In this work, we develop a GQME-based quantum algorithm for simulating the dynamics of an open quantum system. To this end, we develop a protocol for obtaining the non-unitary time evolution superoperator, or propagator, from the memory kernel. Then the Sz.-Nagy unitary dilation theorem is used to convert the GQME-based non-unitary propagator into a unitary superoperator in an extended Hilbert space. Given this dilated and now unitary time evolution superoperator and the initial state of the system, we can evolve the dynamics for any open quantum system on quantum computers.

Given the fact that the GQME is the exact EoM of the open quantum system, this quantum algorithm greatly extends the range of possible systems that can be simulated on a quantum computer, including complex non-Markovian photosynthetic and photovoltaic systems,^{28,73} molecular electronics,⁴⁸ linear and nonlinear spectroscopy,⁷⁴ systems with inter-system crossing,⁷⁵ and conical intersections.⁷⁶ Thus, this GQME-based quantum algorithm

provides an essentially universal protocol for simulating open quantum system dynamics on quantum computing platforms. Given a powerful enough quantum computer, this algorithm opens the door for simulating open quantum system dynamics of large and complex molecular systems, which are currently beyond the reach of classical computers.

2 Methods

2.1 GQME-based propagators

In this section, we outline our approach for calculating the GQME-based non-unitary propagator for the reduced density matrix of the open quantum system (see Eq. (9)). The analogous procedure for calculating the non-unitary propagator for a subset of the reduced density matrix elements is outlined in Sec. 3.2.

Previously developed quantum algorithms for open system dynamics involved mapping Lindblad operators to Kraus operators before using the Sz.-Nagy dilation theorem to reach a unitary quantum algorithm.^{68–70} While useful for many systems, these methods are either Markovian^{68,70} or involve user selection of *ad-hoc* system-bath parameters,⁶⁹ therefore limiting the range of applications. In this paper, we introduce a method based on the GQME, a formally exact EoM for the dynamics of an open quantum system. Instead of casting the non-unitary propagator in terms of Kraus operators and dilating them, this method uses the GQME to obtain the system’s time evolution superoperator, or propagator, $\mathcal{G}(t)$, and perform the dilation on it to obtain a unitary quantum algorithm. This subsection describes the first step in the workflow outlined in Fig. 2, namely obtaining the time evolution superoperator of an open quantum system starting from its formally exact EoM in GQME form.

For the sake of concreteness, we will focus on molecular systems with an overall Hamil-

tonian of the following commonly encountered form:

$$\hat{H} = \sum_{j=1}^{N_e} \hat{H}_j |j\rangle\langle j| + \sum_{\substack{j,k=1 \\ k \neq j}}^{N_e} \hat{V}_{jk} |j\rangle\langle k| \quad (1)$$

and an overall system initial state of the following commonly assumed single-product form:

$$\hat{\rho}(0) = \hat{\rho}_n(0) \otimes \hat{\sigma}(0) \quad . \quad (2)$$

With this assumption, the evolution is guaranteed to be described by a Completely Positive (CP) map.^{60,77} It should be noted that the GQME approach is not limited to this form of Hamiltonian and initial state and that the choice to focus on them is solely motivated by clarity of presentation and the wide range of applications based on an Hamiltonian and an initial state of this form. The system and bath in this case correspond to the electronic and nuclear DOF, respectively. In Eqs. (1) and (2), $\hat{H}_j = \hat{\mathbf{P}}^2/2 + V_j(\hat{\mathbf{R}})$ is the nuclear Hamiltonian when the system is in the diabatic electronic state $|j\rangle$, with the index j running over the N_e electronic states; $\hat{\mathbf{R}} = (\hat{R}_1, \dots, \hat{R}_{N_n})$ and $\hat{\mathbf{P}} = (\hat{P}_1, \dots, \hat{P}_{N_n})$ are the mass-weighted position and momentum operators of the $N_n \gg 1$ nuclear DOF, respectively; $\{\hat{V}_{jk}|j \neq k\}$ are the coupling terms between electronic states (which can be either nuclear operators or constants); and $\hat{\rho}_n(0)$ and $\hat{\sigma}(0)$ are the reduced density operators that describe the initial states of the nuclear (bath) and electronic (system) DOF, respectively. Throughout this paper, boldfaced variables, e.g., \mathbf{A} , indicate vector quantities; a hat over a variable, e.g., \hat{B} , indicates an operator quantity; and calligraphic font, e.g., \mathcal{L} , indicates a superoperator.

Using projection operator techniques, one can then derive the following formally exact EoM, or GQME, for the reduced electronic density operator, $\hat{\sigma}(t)$:^{27–30}

$$\frac{d}{dt} \hat{\sigma}(t) = -\frac{i}{\hbar} \langle \mathcal{L} \rangle_n^0 \hat{\sigma}(t) - \int_0^t d\tau \mathcal{K}(\tau) \hat{\sigma}(t - \tau) \quad . \quad (3)$$

The open quantum system dynamics of the reduced electronic density matrix described by

this GQME is generated by the two terms on the R.H.S. of Eq. (3). The first term is given in terms of the projected overall system Liouvillian $\langle \mathcal{L} \rangle_n^0 \equiv \text{Tr}_n \{ \hat{\rho}_n(0) \mathcal{L} \}$ (where $\mathcal{L}(\cdot) = [\hat{H}, \cdot]$ is the overall system Liouvillian and $\text{Tr}_n \{ \cdot \}$ is the partial trace over the nuclear (bath) Hilbert space), which is represented by a $N_e^2 \times N_e^2$ time-independent matrix. The second term is given in terms of the memory kernel $\mathcal{K}(\tau)$, which is represented by a $N_e^2 \times N_e^2$ time-dependent matrix.

The GQME formalism provides a general framework for deriving the exact EoM for any quantity of interest. The derivation begins with the Nakajima-Zwanzig equation,^{71,72} which describes the dynamics of a projected state $\mathcal{P}\hat{\rho}(t)$, where \mathcal{P} is a projection superoperator and $\hat{\rho}(t)$ is the density operator of the overall system:

$$\begin{aligned} \frac{d}{dt} \mathcal{P}\hat{\rho}(t) = & -\frac{i}{\hbar} \mathcal{P}\mathcal{L}\mathcal{P}\hat{\rho}(t) - \frac{1}{\hbar^2} \int_0^t d\tau \mathcal{P}\mathcal{L}\mathcal{E}^{-i\mathcal{Q}\mathcal{L}\tau/\hbar} \mathcal{Q}\mathcal{L}\mathcal{P}\hat{\rho}(t-\tau) \\ & - \frac{i}{\hbar} \mathcal{P}\mathcal{L}\mathcal{E}^{-i\mathcal{Q}\mathcal{L}t/\hbar} \mathcal{Q}\hat{\rho}(0). \end{aligned} \quad (4)$$

Here, \mathcal{L} is the overall system-bath Liouvillian and $\mathcal{Q} = 1 - \mathcal{P}$ is the complimentary projection superoperator to \mathcal{P} . Importantly, the only requirements are that \mathcal{L} is Hermitian and \mathcal{P} satisfies $\mathcal{P}^2 = \mathcal{P}$. Otherwise, there is complete flexibility in the choice of \mathcal{L} and \mathcal{P} , with each choice leading to a different GQME for a different quantity of interest.³⁰

Following Ref. 27 we focus an overall system-bath Hamiltonian of the form of Eq. (1) and the following choice of projection operator which gives rise to the GQME for the system reduced density matrix, $\hat{\sigma}(t)$:

$$\mathcal{P}(\hat{A}) = \hat{\rho}_n(0) \otimes \text{Tr}_n \{ \hat{A} \}. \quad (5)$$

With this choice of \mathcal{P} , we have $\mathcal{Q}(\hat{\rho}_n(0)) = 0$. Plugging Eq. (5) into Eq. (4) and tracing over the nuclear (bath) Hilbert space leads to the GQME in Eq. (3). The memory kernel in

Eq. (3) is given by

$$\mathcal{K}(\tau) = \frac{1}{\hbar^2} \text{Tr}_n \left\{ \mathcal{L} e^{-i\mathcal{Q}\mathcal{L}\tau/\hbar} \mathcal{Q}\mathcal{L}\hat{\rho}_n(0) \right\}, \quad (6)$$

and can be obtained by solving the following Volterra equation:²⁷

$$\mathcal{K}(\tau) = i\dot{\mathcal{F}}(\tau) - \frac{1}{\hbar} \mathcal{F}(\tau) \langle \mathcal{L} \rangle_n^0 + i \int_0^\tau d\tau' \mathcal{F}(\tau - \tau') \mathcal{K}(\tau'). \quad (7)$$

Here, $\mathcal{F}(\tau)$ and $\dot{\mathcal{F}}(\tau)$ are the so-called projection-free inputs (PFIs), which are given by

$$\begin{aligned} \mathcal{F}(\tau) &= \frac{1}{\hbar} \text{Tr}_n \left\{ \mathcal{L} e^{-i\mathcal{L}\tau/\hbar} \hat{\rho}_n(0) \right\}, \\ \dot{\mathcal{F}}(\tau) &= -\frac{i}{\hbar^2} \text{Tr}_n \left\{ \mathcal{L} e^{-i\mathcal{L}\tau/\hbar} \mathcal{L} \hat{\rho}_n(0) \right\}. \end{aligned} \quad (8)$$

The memory kernels for the spin-boson model used in this paper were adopted from Ref. 78, where they were obtained from quantum-mechanically exact PFIs calculated via the tensor-train thermo-field dynamics (TT-TFD) method.

The quantum open system's *non-unitary* time evolution superoperator, or propagator, $\mathcal{G}(t)$, is defined by:

$$\hat{\sigma}(t) = \mathcal{G}(t) \hat{\sigma}(0) . \quad (9)$$

Substituting Eq. (9) into Eq. (3) and noting that the GQME should be satisfied for an arbitrary choice of $\hat{\sigma}(0)$, it is straightforward to show that $\mathcal{G}(t)$ satisfies the same GQME as $\hat{\sigma}(t)$:

$$\frac{d}{dt} \mathcal{G}(t) = -\frac{i}{\hbar} \langle \mathcal{L} \rangle_n^0 \mathcal{G}(t) - \int_0^t d\tau \mathcal{K}(\tau) \mathcal{G}(t - \tau) . \quad (10)$$

Thus, given the projected Liouvillian and memory kernels ($\langle \mathcal{L} \rangle_n^0$ and $\mathcal{K}(\tau)$, respectively), $\mathcal{G}(t)$ can be obtained by solving Eq. (10) numerically, which in this work was accomplished via a Runge–Kutta fourth-order (RK4) algorithm.²⁸ This superoperator, $\mathcal{G}(t)$, serves a role similar to that of the Kraus operators in the operator sum representation and can also be dilated to

a unitary form which can be implemented on a quantum computer. Importantly, while the Kraus operators are only known in closed form for the Markovian Lindblad equation, the non-unitary propagator $\mathcal{G}(t)$ can always be obtained from the formally exact GQME (see Eq. (10)).

2.2 A GQME-based quantum algorithm for simulating open quantum system dynamics

In this subsection, we describe the next step in the workflow outlined in Fig. 2, namely using the Sz.-Nagy's unitary dilation procedure⁷⁹ to convert the non-unitary quantum open system propagator $\mathcal{G}(t)$ [see Eqs. (9) and (10)] into a unitary propagator in an extended Hilbert space. It should be noted that the Sz.-Nagy unitary dilation procedure is one out of several methods that can convert non-unitary operators into unitary operators (e.g. block-encoding represents an alternative method^{80,81}).

The Sz.-Nagy's unitary dilation procedure starts out by calculating the operator norm of $\mathcal{G}(t)$ to determine if it is a *contraction*. For $\mathcal{G}(t)$ to be a contraction, the operator norm of $\mathcal{G}(t)$ needs to be less than or equal to 1, i.e., $\|\mathcal{G}(t)\|_O = \sup \frac{\|\mathcal{G}(t)v\|}{\|v\|} \leq 1$. In the case where the original $\mathcal{G}(t)$ is *not* a contraction, we introduce a normalization factor $n_c = \|\mathcal{G}(t)\|_O$ in order to define a contraction form of $\mathcal{G}(t)$, namely $\mathcal{G}'(t) = \mathcal{G}(t)/n_c$.

In the next step, we apply a 1-dilation procedure to $\mathcal{G}'(t)$ to obtain a unitary $\mathcal{U}_{\mathcal{G}'(t)}$ in an extended Hilbert space of double the dimension of the original system's Hilbert space:

$$\mathcal{U}_{\mathcal{G}'(t)} = \begin{pmatrix} \mathcal{G}'(t) & \mathcal{D}_{\mathcal{G}'^\dagger(t)} \\ \mathcal{D}_{\mathcal{G}'(t)} & -\mathcal{G}'^\dagger(t) \end{pmatrix}. \quad (11)$$

Here, $\mathcal{D}_{\mathcal{G}'(t)} = \sqrt{I - \mathcal{G}'^\dagger(t)\mathcal{G}'(t)}$ and $\mathcal{D}_{\mathcal{G}'^\dagger(t)} = \sqrt{I - \mathcal{G}'(t)\mathcal{G}'^\dagger(t)}$, where $\mathcal{D}_{\mathcal{G}'(t)}$ is the so-called defect superoperator of $\mathcal{G}'(t)$. The 1-dilation procedure generates a unitary superoperator $\mathcal{U}_{\mathcal{G}'(t)}$ that operates in the extended Hilbert space and replicates the effect of the contraction

form of the original time evolution superoperator, $\mathcal{G}'(t)$, when the input and output vectors are both projected onto the original smaller Hilbert space.

In the original system's Hilbert space, the system reduced density operator $\hat{\sigma}(t)$ is represented by an $N_e \times N_e$ matrix:

$$\hat{\sigma}(t) \doteq \begin{pmatrix} \sigma_{11}(t) & \cdots & \sigma_{1N_e}(t) \\ \vdots & \ddots & \vdots \\ \sigma_{N_e1}(t) & \cdots & \sigma_{N_eN_e}(t) \end{pmatrix}. \quad (12)$$

Alternatively, the same system reduced density operator can also be represented by an N_e^2 -dimensional vector in Liouville space:

$$\hat{\sigma}(t) \doteq (\sigma_{11}(t), \dots, \sigma_{1N_e}(t), \dots, \dots, \sigma_{N_e1}(t), \dots, \sigma_{N_eN_e}(t))^T. \quad (13)$$

Since the GQME formalism is given in terms of superoperators, it is convenient to work in Liouville space, which we will do from this point on. We also define the norm of the vector representing $\hat{\sigma}(t)$ in Liouville space as the Frobenius norm: $\|\sigma(t)\|_F = \sqrt{\sum_{ij} |\sigma_{ij}|^2}$ and divide $\hat{\sigma}(t)$ by $\|\sigma(t)\|_F$ to normalize $\hat{\sigma}(t)$.⁶⁸

Given the dilated unitary operator $\mathcal{U}_{\mathcal{G}'(t)}$ and the initial quantum input state $\hat{\sigma}(0)$, operating with the non-unitary $\mathcal{G}'(t)$ on $\hat{\sigma}(0)$ has now been converted into a unitary transformation as follows:

$$\mathcal{G}'(t)\hat{\sigma}(0) \xrightarrow{\text{unitary dilation}} \mathcal{U}_{\mathcal{G}'(t)} (\hat{\sigma}(0)^T, 0, \dots, 0)^T. \quad (14)$$

The 0s in the input vector on the R.H.S. are added to match the dimension of the input vector with that of $\mathcal{U}_{\mathcal{G}'(t)}$. The unitary process can then be simulated on a quantum circuit with unitary quantum gates. The electronic populations, $\{\sigma_{jj}(t) \equiv \langle j|\hat{\sigma}(t)|j\rangle | j = 1, \dots, N_e\}$ can be retrieved by taking the square roots of the probability of measuring each basis state $P_j(t) = |\sigma'_{jj}(t)|^2$ and multiplying by the n_c factor.

Finally, we perform a complexity analysis of the quantum algorithm. Given that $\mathcal{G}(t)$

in its most general form is represented by a matrix of N_e^4 non-zero elements, the defect superoperators $\mathcal{D}_{\mathcal{G}'}(t)$ as well as $-\mathcal{G}^\dagger(t)$ as shown in Eq. (11) all have N_e^4 non-zero elements. Generally speaking, the number of the two-level unitaries necessary to decompose a unitary gate is comparable to the number of non-zero elements in the lower-triangular part of the gate.^{82,83} Therefore, the gate complexity to simulate this specific $\mathcal{U}_{\mathcal{G}'}(t)$ is $O(N_e^4)$. If the two-level unitaries are further decomposed into 1-qubit and 2-qubit elementary gates commonly used to design conventional quantum circuits, they need to be transformed to the Gray code sequences and some multi-control gate sequences, adding another factor of complexity logarithmic in N_e^2 , and the total complexity becomes $O(N_e^4 \log^2 N_e^2)$.⁸² This means that the maximum total complexity of a GQME-based simulation of an open quantum system dynamics is comparable to classical methods.⁶⁸ However, as demonstrated in previous simulations of certain dynamical models, our quantum algorithm can take advantage of the case when the $\mathcal{G}(t)$ is a sparse matrix, and thus the gate complexity scaling for $\mathcal{G}(t)$ can be reduced to $O(\log^2 N_e^2)$ instead of $O(N_e^4)$.^{68,70}

3 Results

3.1 A demonstrative application to the spin-boson model

In this subsection, we test the applicability of the quantum algorithm outlined in the previous sections on the spin-boson benchmark model. This model and its derivatives have a wide range of applicability to chemical and physical systems, including electron, proton, energy, and charge transfer processes; polaron formation and dynamics in condensed phase environments; vibrational relaxation, impurity relaxation in solids, spin-lattice relaxation, and qubit decoherence.^{22,23,84,85} It should also be noted that quantum-mechanically exact memory kernels for this model are available.^{78,86,87}

The spin-boson Hamiltonian has the form of Eq. (1) with $N_e = 2$ and $\{\hat{H}_j, \hat{V}_{jk}\}$ given by:

$$\begin{aligned}
\hat{H}_0 &\equiv \hat{H}_D = \epsilon + \sum_{k=1}^{N_n} \frac{\hat{P}_k^2}{2} + \frac{1}{2} \omega_k^2 \hat{R}_k^2 - c_k \hat{R}_k, \\
\hat{H}_1 &\equiv \hat{H}_A = -\epsilon + \sum_{k=1}^{N_n} \frac{\hat{P}_k^2}{2} + \frac{1}{2} \omega_k^2 \hat{R}_k^2 + c_k \hat{R}_k, \\
\hat{V}_{01} &\equiv \hat{V}_{DA} = \hat{V}_{10} \equiv \hat{V}_{AD} = \Gamma.
\end{aligned} \tag{15}$$

Here, the two electronic states are designated as the donor and acceptor ($|D\rangle$ and $|A\rangle$, respectively), 2ϵ is the shift in equilibrium energy between the donor (D) and acceptor (A) states, and Γ is a positive constant describing the electronic coupling between the donor and acceptor states. Since Γ is a constant, this system is assumed to satisfy the Condon approximation.

The results shown below were obtained for the case where the nuclear modes' frequencies and coupling coefficients $\{\omega_k, c_k\}$ are sampled from an Ohmic spectral density with exponential cutoff:

$$J(\omega) = \frac{\pi}{2} \sum_{k=1}^{N_n} \frac{c_k^2}{\omega_k} \delta(\omega - \omega_k) \xrightarrow{N_n \rightarrow \infty} \frac{\pi \hbar}{2} \xi \omega e^{-\omega/\omega_c} . \tag{16}$$

Here, ξ is the Kondo parameter and ω_c is the cutoff frequency. The reader is referred to Appendix C of Ref. 27 for a description of the procedure used to obtain a discrete set of N_n nuclear mode frequencies $\{\omega_k\}$ and coupling coefficients $\{c_k\}$ from the spectral density in Eq. (16).

The initial state is assumed to be of the form of Eq. (2), with the initial electronic (system) reduced density operator given by

$$\hat{\sigma}(0) = |D\rangle\langle D| \tag{17}$$

Table 1: Spin-boson model and simulation parameters.

Model #	Model Parameters					Numerical Parameters		
	ϵ	Γ	β	ξ	ω_c	ω_{\max}	N_n	Δt
1	1.0Γ	1.0	$5.0 \Gamma^{-1}$	0.1	1.0Γ	5Γ	60	$1.50083 \times 10^{-3} \Gamma^{-1}$
2	1.0Γ	1.0	$5.0 \Gamma^{-1}$	0.1	2.0Γ	10Γ	60	$1.50083 \times 10^{-3} \Gamma^{-1}$
3	1.0Γ	1.0	$5.0 \Gamma^{-1}$	0.4	2.0Γ	10Γ	60	$1.50083 \times 10^{-3} \Gamma^{-1}$
4	0.0Γ	1.0	$5.0 \Gamma^{-1}$	0.2	2.5Γ	12Γ	60	$4.50249 \times 10^{-3} \Gamma^{-1}$

and the initial nuclear (bath) reduced density operator given by

$$\hat{\rho}_n(0) = \frac{e^{-\beta(\hat{H}_D + \hat{H}_A)/2}}{\text{Tr}_n \left\{ e^{-\beta(\hat{H}_D + \hat{H}_A)/2} \right\}}. \quad (18)$$

Calculations were carried out for four different sets of parameter values (see Table 1). Models 1 and 2 correspond to systems with an energy bias between the donor and acceptor states ($\epsilon \neq 0$) and differ in their cutoff frequencies, with model 2 having a higher cutoff frequency. Model 3 corresponds to a biased system with the same parameters as model 2 except for a larger Kondo parameter. Model 4 corresponds to a symmetric system with zero energy bias between the donor and acceptor states ($\epsilon = 0$). The results reported in this paper were obtained with a time step of $\Delta t = 1.50083 \times 10^{-3} \Gamma^{-1}$ for models 1-3 and a time step of $\Delta t = 4.50249 \times 10^{-3} \Gamma^{-1}$ for model 4.

Starting with the quantum-mechanically exact memory kernels (adopted from Ref. 78), the time evolution superoperator for the electronic reduced density matrix $\mathcal{G}(\tau)$ was generated for the four models given in Table 1 by solving the corresponding GQME, Eq. (10).

The GQME-based quantum algorithm for simulating the electronic dynamics within the spin-boson model was implemented on the IBM quantum platforms via the Qiskit package.⁸⁸ The quantum implementation involved the translation of $\mathcal{G}'(t)$ into $\mathcal{U}_{\mathcal{G}'}(t)$ at each time step, followed by the construction of a quantum circuit based on $\mathcal{U}_{\mathcal{G}'}(t)$, and lastly the use of the quantum circuit to simulate the time evolution of the reduced electronic density matrix. To build the circuit, we dilated the 4×4 $\mathcal{G}'(t)$ into a unitary 8×8 $\mathcal{U}_{\mathcal{G}'}(t)$ by using a 1-dilation

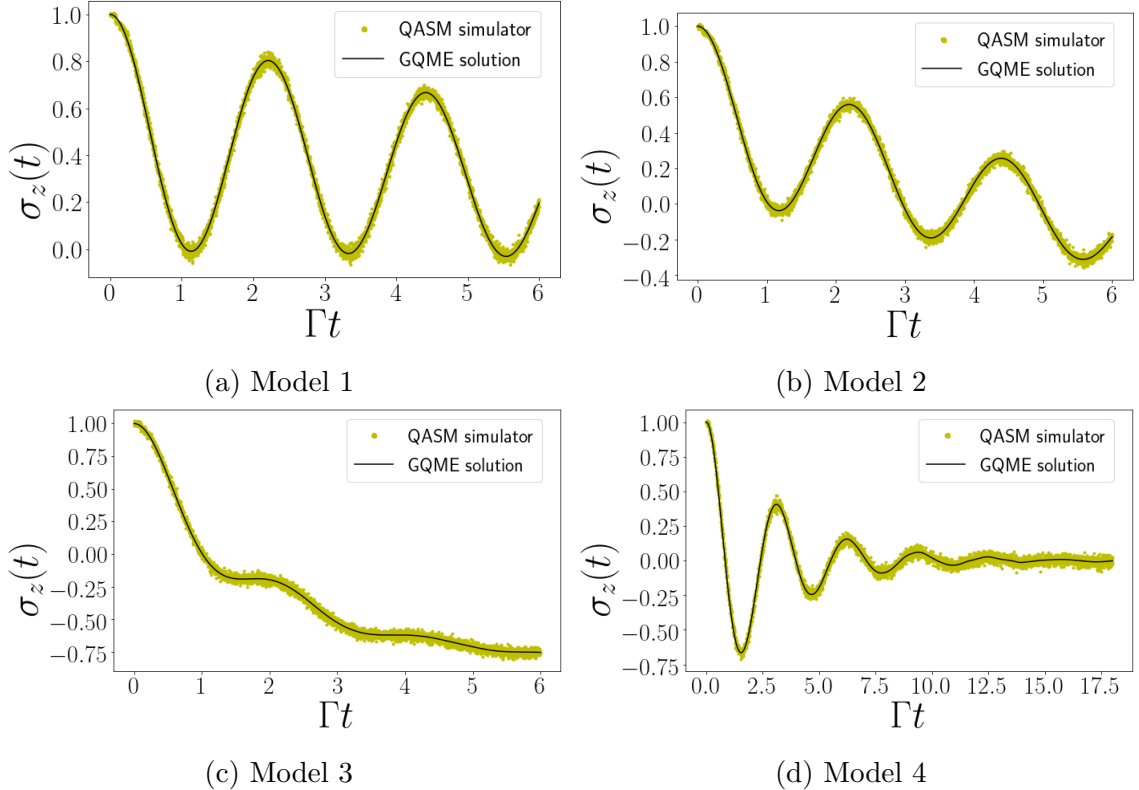


Figure 3: The spin-boson model simulated by the GQME-based quantum algorithm as implemented on the IBM QASM quantum simulator, showing the electronic population difference between the donor state and acceptor state $\sigma_z(t) = \sigma_{DD}(t) - \sigma_{AA}(t)$ as a function of time for (a) model 1, (b) model 2, (c) model 3, and (d) model 4 as given in Table 1, with units scaled to the electronic coupling, Γ . Each figure shows the comparison between the GQME-based exact results represented by the black curves and the QASM-based results represented by the yellow dots. The time step for both the exact and simulated results is $\Delta t = 1.50083 \times 10^{-3} \Gamma^{-1}$ for models 1-3 and $\Delta t = 4.50249 \times 10^{-3} \Gamma^{-1}$ for model 4. Each model is simulated for 4000 time steps. The number of projection measurements applied by the QASM simulator to obtain a single time step is 2000 shots.

procedure [see Eq. (11)]. The unitary $\mathcal{U}_{G'}(t)$ was then transpiled into a 3-qubit quantum circuit composed of three elementary quantum gates: R_Z , \sqrt{X} , and CX . Examples of $\mathcal{U}_{G'}(t)$ and details of the elementary quantum gates and circuits are given in the supplementary information (SI). The initial electronic state is set to $(1, 0, 0, 0, 0, 0, 0, 0)^T$, where the last four 0s are the extra dimensions from the dilation procedure. The QASM simulator and the real quantum devices initialize the input state $(1, 0, 0, 0, 0, 0, 0, 0)^T$ and apply the unitary operation $\mathcal{U}_{G'}(t)$ to the input state followed by projection measurements to retrieve the

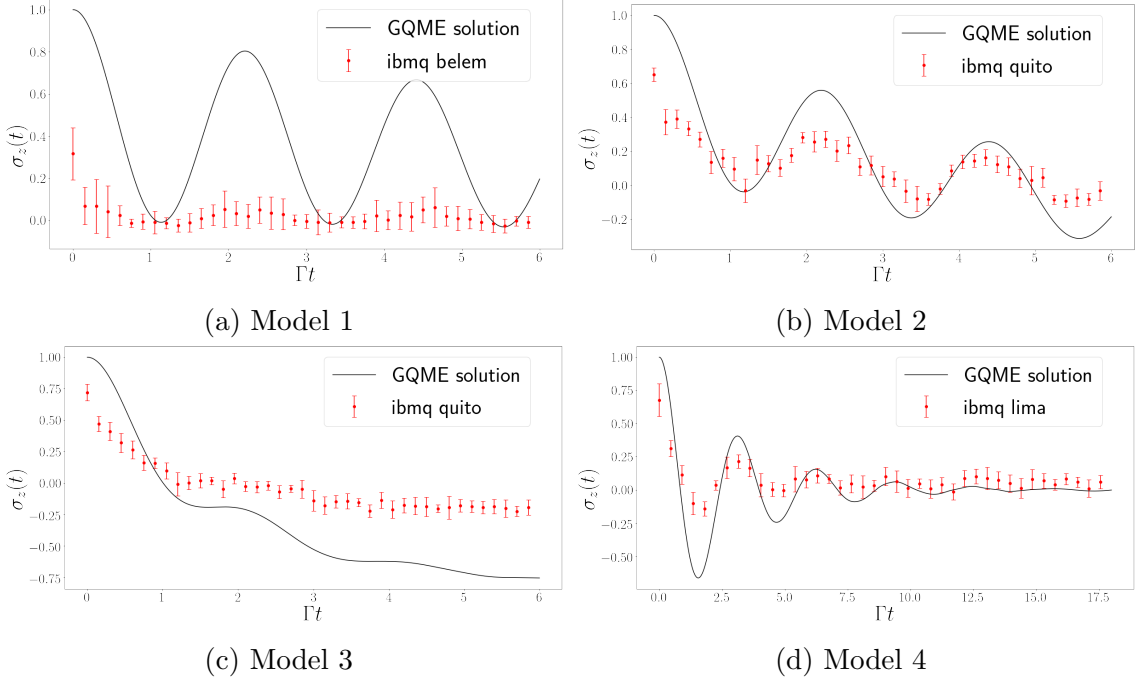


Figure 4: The spin-boson model simulated by the GQME quantum algorithm as implemented on the IBM quantum computers **ibmq belem**, **ibmq quito** and **ibmq lima**, showing the electronic population difference between the donor state and acceptor state $\sigma_z(t) = \sigma_{DD}(t) - \sigma_{AA}(t)$ as a function of time for (a) model 1 , (b) model 2 (c) model 3 and (d) model 4 as given in Table 1, with units scaled to the electronic coupling, Γ . Each figure shows the comparison between the GQME-based exact results represented by the black curves and quantum-computer-based results represented by the red dots with error bars. The time step for the real machine simulation is $\Delta t = 0.150083 \Gamma^{-1}$ for model 1,2 and 3 and $\Delta t = 0.450249 \Gamma^{-1}$ for model 4. The experiments of both models take 40 evenly-spaced time steps out of the 4000 time steps used in the QASM simulator runs and the error bars represent the standard derivations of the 10 separate runs on the **ibmq belem**, **ibmq quito** and **ibmq lima** for models 1 to 4. The number of projection measurements applied by all the devices to obtain a single time step is 2000 shots.

probability distribution of all the 8 basis states. Each circuit runs 2000 shots and the resulting probabilities $P_{000}(t)$ of measuring the state $|000\rangle$ and $P_{011}(t)$ of measuring $|011\rangle$ correspond to the diagonal elements of the modified density matrix $|\sigma'_{00}(t)|^2$ and $|\sigma'_{11}(t)|^2$. The populations of the donor state, $\sigma_{00}(t)$, and acceptor state, $\sigma_{11}(t)$, are retrieved as follows:

$$\sigma_{00}(t) = \sqrt{P_{000}(t)} \times n_c \text{ and } \sigma_{11}(t) = \sqrt{P_{011}(t)} \times n_c . \quad (19)$$

In what follows, we report results in terms of the difference between the donor and acceptor

populations, $\sigma_z(t) = \sigma_{00}(t) - \sigma_{11}(t)$.

The comparison between the exact results obtained by solving the GQME on a classical computer and results obtained by performing the quantum algorithm on the QASM simulator is shown in Fig. 3. The QASM simulator results are in excellent agreement with the exact results for all four models under consideration. The small amplitude oscillations of the QASM-based results around the exact results can be traced back to the inherent uncertainty associated with projection measurements. These results validate the GQME-based quantum algorithm and demonstrate its ability to reproduce results obtained via the GQME-based classical algorithm.

To test the performance of the quantum algorithm on real quantum devices, we also performed the simulations on the quantum computers provided by IBM Quantum (IBM Q). The simulations were performed for models 1 to 4 on **ibmq quito**, **ibmq belem** and **ibmq lima**. All devices are equipped with 5 qubits that have the same qubit connectivity and use IBM's **Falcon r4T** processor with the same architecture. In each simulation of a given model, three qubits were used and 10 repeated experiments were performed. In a single experiment, 40 time steps are chosen at an equal spacing out of the 4000 time steps used in the QASM simulations, i.e., the time step in each experiment is 100 times greater than the time step used in the QASM simulations as listed in Table 1. The average CX gate error and readout error are $(1.191 \times 10^{-2}, 5.194 \times 10^{-2})$ for the **ibmq quito**, $(1.160 \times 10^{-2}, 2.590 \times 10^{-2})$ for the **ibmq belem** and $(1.032 \times 10^{-2}, 2.834 \times 10^{-2})$ for the **ibmq lima** as of the time of the experiments. The quantum circuits are the same in both the QASM simulations and the real machine simulations. The transpiled quantum gate counts for each of the $\mathcal{U}_{G'}(t)$ superoperators are 153 R_Z gates, 98 \sqrt{X} gates, and 41 CX gates. The transpiling process is done internally by the Qiskit package and examples of the quantum circuits can be found in the SI.

The comparison between the GQME-generated exact results and real machine simulations is given in Fig. 4. In the figure, the red dots are the average of the 10 experiments and the

error bars represent standard derivations of the 10 experiments. While the results obtained on the IBM Q quantum computers reproduce some of the trends exhibited by the exact results, the agreement is qualitative at best. The lack of quantitative agreement can be traced back to the rather extensive circuit depth, which makes the calculation susceptible to noise. In the next section, we propose a way to lower the circuit depth and enhance the accuracy of the calculation on the IBM Q quantum computers by using reduced-dimensionality GQMEs.

3.2 Reduced-dimensionality GQME-based propagators

Since the quantum algorithm on the QASM simulator was able to accurately reproduce the exact results, as shown in Fig. 3, we attribute the lack of quantitative agreement between the exact results and the results obtained via the IBM Q quantum computers, as seen in Fig. 4, to noise within the real quantum devices. If so, reducing the circuit depth would improve the accuracy. In this subsection, we validate this hypothesis by reducing the dimensionality of the non-unitary propagator $\mathcal{G}(t)$, and thereby lowering the circuit depth to levels that allow for an accurate calculation on the NISQ quantum computers.

To this end, we take inspiration from reduced-dimensionality GQMEs, which correspond to EoMs for subsets of the open quantum system's reduced density matrix elements, rather than the full reduced density matrix.^{30,78} For example, for the spin-boson model described in Sec. 3.1, the memory kernel in the GQME for the full reduced density matrix, $\hat{\sigma}(t)$, is a 4×4 matrix, while the memory kernel in the GQME for only the two populations (the diagonal elements of the reduced density matrix, $\sigma_{00}(t)$ and $\sigma_{11}(t)$) is a 2×2 matrix.^{30,78} Below, we demonstrate how one can take advantage of this reduced dimensionality to lower the circuit depth and thereby improve the accuracy of the simulation on quantum machines.

For the spin-boson model under consideration in this paper, the electronic populations

can be propagated using only the four corner elements of $\mathcal{G}(t)$, i.e.,

$$\begin{pmatrix} \sigma_{11}(t) \\ \sigma_{22}(t) \end{pmatrix} = \begin{pmatrix} \mathcal{G}_{11,11}(t) & \mathcal{G}_{11,22}(t) \\ \mathcal{G}_{22,11}(t) & \mathcal{G}_{22,22}(t) \end{pmatrix} \begin{pmatrix} \sigma_{11}(0) \\ \sigma_{22}(0) \end{pmatrix}. \quad (20)$$

It should be noted that this equality only holds when the initial electronic state is of the form $\hat{\sigma}(0) = \sum_{j=1}^{N_e} \sigma_{jj}(0)|j\rangle\langle j|$, which is consistent with the initial state under consideration in this paper (see Eq. (17)). It should also be noted that Eq. (20) is still exact, in the sense that the time evolution of $\sigma_{11}(t)$ and $\sigma_{00}(t)$ as described by the equation is exactly the same time evolution as described by Eq. (9). Thus, the only price one pays for the reduced dimensionality is the loss of the ability to simulate the dynamics of the off-diagonal matrix elements $\sigma_{10}(t)$ and $\sigma_{01}(t)$. However, given that the primary goal is often to simulate the dynamics of electronic energy/charge transfer, the populations of the corresponding electronic states is all that one needs. Finally, it is worth noting that our specific way of choosing the subset of the density operator does not indicate there is no coupling between the elements. In fact, such coupling can be captured exactly by the memory kernel and the effective Liouvillian of any open quantum system with the GQME.

The 2×2 propagator in Eq. (20), which we will refer to as $\mathcal{G}^{\text{pop}}(t)$, can be dilated following a procedure similar to that we used to dilate the 4×4 propagator for the full density matrix, $\mathcal{G}(t)$. More specifically, $\mathcal{G}^{\text{pop}}(t)$ can be divided by a normalization factor $n_c^{\text{pop}} = \|\mathcal{G}^{\text{pop}}(t)\|_O$ to obtain its contraction form $\mathcal{G}^{\text{pop}'}(t) = \mathcal{G}^{\text{pop}}(t)/n_c^{\text{pop}}$. Applying a 1-dilation procedure to $\mathcal{G}^{\text{pop}'}(t)$, similar to that in Eq. (11), then leads to the following unitary propagator:

$$\mathcal{U}_{\mathcal{G}^{\text{pop}'}}(t) = \begin{pmatrix} \mathcal{G}^{\text{pop}'}(t) & \mathcal{D}_{\mathcal{G}^{\text{pop}'}}(t) \\ \mathcal{D}_{\mathcal{G}^{\text{pop}'}}(t) & -\mathcal{G}^{\text{pop}'\dagger}(t) \end{pmatrix}. \quad (21)$$

Notably, for the spin-boson model, while $\mathcal{U}_{\mathcal{G}'}(t)$ is an 8×8 time-dependent matrix, $\mathcal{U}_{\mathcal{G}^{\text{pop}'}}(t)$ is a 4×4 time-dependent matrix.

A comparison between the exact results and results obtained by performing the quantum algorithm based on Eq. (21) on IBM Q quantum machines is shown in Fig. 5. The results shown were obtained for models 1-4 on **ibmq belem**, **ibmq lima**, **ibm oslo** and **ibm nairobi**, respectively. Here, **ibm oslo** and **ibm nairobi** are each equipped with 7 qubits of the same qubit connectivity and both use IBM’s **Falcon r5.11H** processor. The average CX gate error and readout error are $(1.038 \times 10^{-2}, 2.280 \times 10^{-2})$ for the **ibm nairobi** and $(8.537 \times 10^{-3}, 2.310 \times 10^{-2})$ for the **ibm oslo** as of the time of the experiments. The new simulations use the same time steps, experiment shots and follow the same procedures as that used to obtain the results in Fig. 4. The quantum circuits are re-transpiled to implement the reduced-dimensionality GQME-based quantum algorithm where only two qubits are used. The transpiled quantum gate counts for each of the $\mathcal{U}_{G^{pop}}(t)$ superoperators are 17 R_Z gates, 12 \sqrt{X} gates, and 2 CX gates. The transpiling processes are done internally by the Qiskit package.

The results in Fig. 5 confirm that the lack of quantitative agreement seen in Fig. 4 can be attributed to noise on the real quantum devices. More specifically, significantly more accurate results are obtained when the populations-only reduced dimensionality GQME-based propagators are used, which can be traced back to their ability to give rise to shallower quantum circuits. Thus, reduced dimensionality make it possible to accurately simulate the open quantum system dynamics on NISQ quantum computers.

4 Concluding Remarks

The GQME-based quantum algorithm proposed herein substantially expands the range of open quantum systems that can be simulated on a quantum computer. In this paper, we demonstrated the applicability and versatility of the algorithm by using it to simulate the dynamics of electronic populations within the benchmark spin-boson model on the IBM QASM quantum simulator and IBM quantum computers.

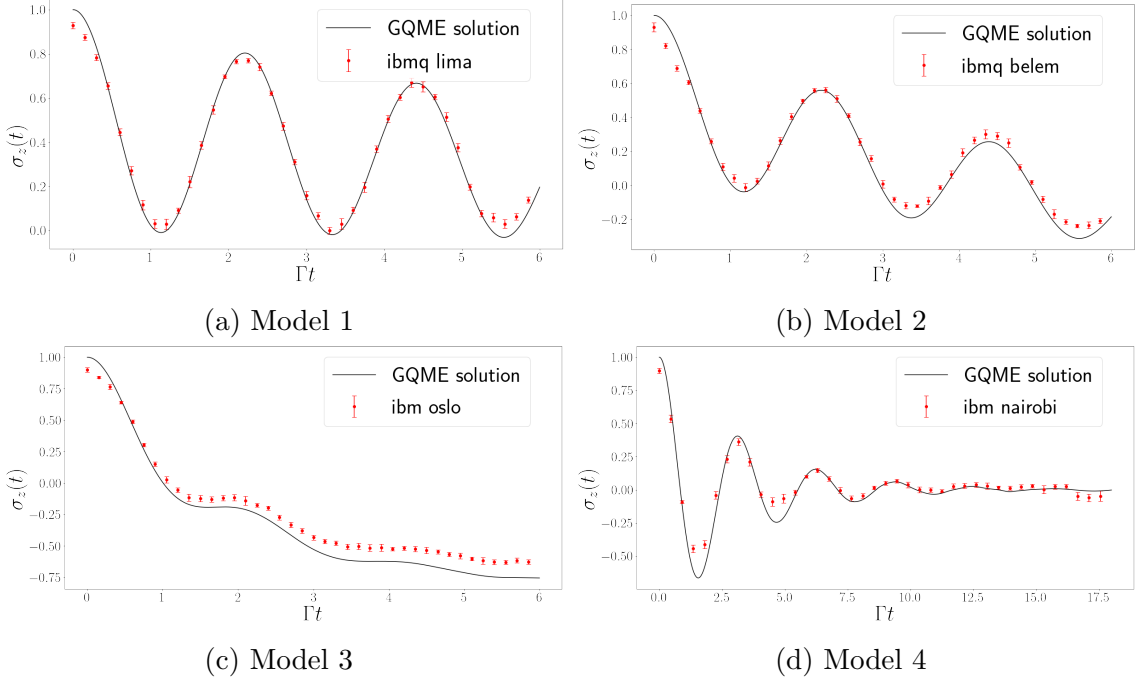


Figure 5: A comparison between the exact results for the spin-boson model and results obtained by performing the quantum algorithm based on Eq. (21) on the IBM Q quantum machines. The electronic population difference between the donor state and acceptor state, $\sigma_z(t) = \sigma_{DD}(t) - \sigma_{AA}(t)$, is plotted as a function of time for (a) model 1, (b) model 2 (c) model 3 and (d) model 4 as given in Table 1, with units scaled to the electronic coupling, Γ . Each panel shows the comparison between the exact results represented by the black curves and the population-only-QGME-based quantum-computer-simulated results represented by the red dots with error bars. The time step for the real machine simulation is $\Delta t = 0.150083 \Gamma^{-1}$ for model 1, 2 and 3 and $\Delta t = 0.450249 \Gamma^{-1}$ for model 4. The experiments of both models take 40 evenly-spaced time steps out of the 4000 time steps used in the QASM simulator runs and the error bars represent the standard deviations of the 10 separate runs on the **ibmq lima**, **ibmq belem**, **ibm oslo** and **ibm nairobi** for models 1-4, respectively. The number of projection measurements applied by all the devices to simulate a single time step is 2000 shots.

The results obtained via the noise-free QASM simulator were found to be highly accurate, with the only errors inherently associated with the quantum projection measurements and giving rise to very slight deviations from the exact results. However, while the implementation of the algorithm on the NISQ IBM Q quantum computers was found to reproduce some of the trends exhibited by the exact results, the agreement was qualitative at best. This lack of quantitative agreement was traced back to the rather extensive circuit depth, which made the calculation susceptible to noise. This issue was confirmed and fixed by

implementing a populations-only reduced-dimensionality version of the quantum algorithm, which significantly shortened the circuit depth and as a result gave rise to quantitatively accurate results.

We acknowledge the fact that demonstrating quantum advantage is currently challenging for the proposed quantum algorithm used to simulate open quantum dynamics. However, quantum dynamics simulations often become computationally intractable on a classical computer even when the propagator is known (or numerically determined). This is simply because the time evolving state becomes highly entangled and therefore requires an exponentially large N memory space, with N the number of possible states in Hilbert space (and an exponentially large computational effort). In contrast, a quantum computer can efficiently represent the time-evolving state with only $\log_2(N)$ qubits. In addition, further improvement to our quantum simulations can be achieved by reducing the circuit depth via optimizing the quantum circuit design. This can be achieved by optimizing the decomposition of unitary operations into elementary gate sequences.^{89–92} One particularly interesting idea is to reduce the circuit depth by adding qubits.⁹³ To this end, it should be noted that we have only used 3 qubits out of the 5 currently available on the IBM quantum computers. Another way for improving accuracy is by active error correction using dynamical decoupling (DD) protocols, that employ pulses to suppress the system’s coupling with the environment.^{94–98} Recent implementations of DD on IBM machines was found to improve the fidelity of the overall performance.^{99–101} Yet another direction is to implement the circuit on high-dimensional qudit machines. Quantum computers based on three-dimensional circuit quantum electrodynamics (3D cQED) microwave cavities are particularly promising in this respect, as they feature unique quantum error correction schemes^{102–104} and longer coherence times^{105,106} than standard superconducting quantum computers. Bosonic quantum computing algorithms have also been recently shown to significantly reduce the number of quantum gates required for the calculation of the Franck-Condon factors¹⁰⁷ and dynamics of rhodopsin near conical intersections.¹⁰⁸ Lossless 3D cQED systems have not yet been employed to simulate open

quantum system dynamics. An adaptation of the algorithm presented here to bosonic quantum computing could therefore provide another way to efficiently simulate open quantum system dynamics and demonstrate how qudit-based quantum architectures can reduce the computational cost and enhance the accuracy of quantum simulations.

A Quantum circuit examples

In this section, we include further details concerning the quantum algorithm, including the dilation process, circuit transpiling, QASM simulations, and simulations running on the IBM quantum computers **ibmq quito** and **ibmq lima**. The normalized time evolution operator of the electronic reduced density operator $\mathcal{G}'(t) = \mathcal{G}(t)/n_c$ (where $\mathcal{G}(t)$ is generated from the GQME formalism) is dilated into a unitary operator $\mathcal{U}_{\mathcal{G}'(t)}$. We start with \mathcal{G}_3 , which corresponds to the $\mathcal{G}(t)$ of the 1500th time step from model 3, and \mathcal{G}_4 , which corresponds to the $\mathcal{G}(t)$ of the 1500th time step from model 4. The matrix of \mathcal{G}_3 and \mathcal{G}_4 are, respectively:

$$\mathcal{G}_3 = \begin{pmatrix} 0.38 - 3.76 \times 10^{-10}j & 0.04 + 2.90 \times 10^{-2}j & 0.04 - 2.90 \times 10^{-2}j & 0.06 - 1.88 \times 10^{-10}j \\ -0.13 + 7.04 \times 10^{-2}j & 0.28 - 2.63 \times 10^{-2}j & 0.02 + 2.37 \times 10^{-2}j & -0.15 - 3.06 \times 10^{-2}j \\ -0.13 - 7.04 \times 10^{-2}j & 0.02 - 2.37 \times 10^{-2}j & 0.28 + 2.63 \times 10^{-2}j & -0.15 + 3.06 \times 10^{-2}j \\ 0.62 + 3.77 \times 10^{-10}j & -0.04 - 2.90 \times 10^{-2}j & -0.04 + 2.90 \times 10^{-2}j & 0.94 + 1.87 \times 10^{-10}j \end{pmatrix}, \quad (22)$$

and

$$\mathcal{G}_4 = \begin{pmatrix} 0.54 + 4.7 \times 10^{-11}j & -1.7 \times 10^{-6} + 5.7 \times 10^{-2}j & -1.6 \times 10^{-6} - 5.6 \times 10^{-2}j & 0.46 + 7.1 \times 10^{-11}j \\ -0.46 + 5.7 \times 10^{-2}j & 3.6 \times 10^{-2} + 6.1 \times 10^{-5}j & -1.6 \times 10^{-2} - 5.7 \times 10^{-5}j & -0.46 - 5.7 \times 10^{-2}j \\ -0.46 - 5.7 \times 10^{-2}j & -1.6 \times 10^{-2} + 5.7 \times 10^{-5}j & 3.7 \times 10^{-2} - 6.1 \times 10^{-5}j & -0.46 + 5.7 \times 10^{-2}j \\ 0.54 - 4.7 \times 10^{-11}j & 1.6 \times 10^{-6} - 5.6 \times 10^{-2}j & 1.6 \times 10^{-6} + 5.6 \times 10^{-2}j & 0.54 - 7.1 \times 10^{-11}j \end{pmatrix}. \quad (23)$$

The normalization factors used for model 3 and model 4 are $n_{c3} = 1.376$ and $n_{c4} = 1.376$.

Following the 1-dilation process, the 4×4 $\mathcal{G}'(t)$ [derived from corresponding $\mathcal{G}(t)$ divided by the n_c factor] is converted into a unitary 8×8 $\mathcal{U}_{\mathcal{G}'(t)}$. We show $\mathcal{U}_{\mathcal{G}'_3}$ and $\mathcal{U}_{\mathcal{G}'_4}$ in the form of heat maps in Fig. 6.

The unitary operation $\mathcal{U}_{\mathcal{G}'(t)}$ is transpiled into a 3-qubit quantum circuit composed of

three elementary quantum gates: R_Z , \sqrt{X} , and CX , which have the matrix form:

$$R_Z(\lambda) = \exp\left(-i\frac{\lambda}{2}Z\right) = \begin{pmatrix} e^{-i\frac{\lambda}{2}} & 0 \\ 0 & e^{i\frac{\lambda}{2}} \end{pmatrix} \quad (24)$$

$$\sqrt{X} = \frac{1}{2} \begin{pmatrix} 1+i & 1-i \\ 1-i & 1+i \end{pmatrix} \quad (25)$$

$$CX_{q_0, q_1} = I \otimes |0\rangle\langle 0| + X \otimes |1\rangle\langle 1| = \begin{pmatrix} 1 & 0 & 0 & 0 \\ 0 & 0 & 0 & 1 \\ 0 & 0 & 1 & 0 \\ 0 & 1 & 0 & 0 \end{pmatrix} \quad (26)$$

The full quantum circuits for \mathcal{U}_{G_3} and \mathcal{U}_{G_4} are shown in Fig. 8 and 9. The probability distribution of the projection measurement results of the two circuits are shown in Fig. 7. Both the QASM simulator results and the real machine simulated results are recorded.

B Amplitude-damping model

In this section, we will show that the method of flattening the density matrix for dilation, which was outlined in the supplementary information in our previous publication,⁶⁸ can be implemented on the quantum device for the simple amplitude damping model. The same method is verified by the implementation described in this and the following section. This verification allows us to confidently incorporate the general algorithm with GQME.

The general algorithm for open quantum system dynamics is applicable to the time-evolution of density matrices governed by Kraus operators.⁶⁸ The time-evolution representation for such open systems is given by $\hat{\rho}(t) = \sum_k \mathcal{M}_k(t)\hat{\rho}\mathcal{M}_k^\dagger(t)$. For simplicity, the notation of time dependency is omitted hereafter for superoperators \mathcal{M} and superoperators derived from it. In the first step, the density matrix is flattened to vector form: $\hat{\rho} \rightarrow \mathbf{v}_\rho = (\rho_{11}, \dots, \rho_{1n}, \rho_{21}, \dots, \rho_{2n}, \dots, \rho_{n1}, \dots, \rho_{nn})^T$. We calculate the Frobenius norm of \mathbf{v}_ρ

as $\|\mathbf{v}_\rho\|_F = \sqrt{\sum_{ij} |\rho_{ij}|^2}$ and divide \mathbf{v}_ρ by $\|\mathbf{v}_\rho\|_F$ to normalize \mathbf{v}_ρ . Next, for every k , the \mathcal{M}_k is transformed into $\tilde{\mathcal{M}}_k = \mathcal{M}_k \otimes I$; similarly, the \mathcal{M}_k^\dagger is transformed into $\tilde{\mathcal{N}}_k = I \otimes \bar{\mathcal{M}}_k$. The \otimes stands for the Kronecker product and the bar over \mathcal{M}_k indicates complex conjugation. The new equivalent form for the Kraus representation is:

$$\mathcal{M}_k \hat{\rho} \mathcal{M}_k^\dagger \xleftrightarrow{\text{equivalent}} \tilde{\mathcal{N}}_k \tilde{\mathcal{M}}_k \mathbf{v}_\rho. \quad (27)$$

The input state is initialized to the normalized \mathbf{v}_ρ in the execution. In Ref. 68, it is shown that the Kraus operator \mathcal{M}_k is a contraction. Therefore $\tilde{\mathcal{M}}_k = \mathcal{M}_k \otimes I$ and $\tilde{\mathcal{N}}_k = I \otimes \bar{\mathcal{M}}_k$ are also contractions as per the norm property of the Kronecker product. To build the quantum circuit of $\tilde{\mathcal{N}}_k \tilde{\mathcal{M}}_k \mathbf{v}_\rho$ with unitary gates, we need two separate 2-dilations:

$$\tilde{\mathcal{N}}_k \tilde{\mathcal{M}}_k \mathbf{v}_\rho \xrightarrow{\text{unitary dilation}} \mathcal{U}_{\mathcal{N}_k} \mathcal{U}_{\mathcal{M}_k} (\mathbf{v}_\rho^T, 0, \dots, 0)^T. \quad (28)$$

For \mathcal{M}_k of dimension $n \times n$, $\tilde{\mathcal{M}}_k$ and $\tilde{\mathcal{N}}_k$ are $n^2 \times n^2$; and consequently, the 2-dilations $\mathcal{U}_{\mathcal{M}_k}$ and $\mathcal{U}_{\mathcal{N}_k}$ are $3n^2 \times 3n^2$. The $\mathcal{U}_{\mathcal{M}_k}$ and $\mathcal{U}_{\mathcal{N}_k}$ are fragmented into sequences of two-level unitary gates and tallied to compute the gate complexity. To realize $\tilde{\mathcal{N}}_k \tilde{\mathcal{M}}_k \mathbf{v}_\rho$, the total gate complexity is $3n^3 + n^2$ for each k . The classical complexity to realize $\mathcal{M}_k \hat{\rho} \mathcal{M}_k^\dagger$ based on a naive algorithm is higher, though of same order as quantum algorithm, namely $4n^3 - 2n^2$.

All the evolved density matrices in the circuit calculated at each timestep are obtained as the output vector $\mathbf{v}_k(t) = \tilde{\mathcal{N}}_k \tilde{\mathcal{M}}_k \mathbf{v}_\rho$. The desired information to be collected from the density matrix is extracted by applying projection measurements on $\mathbf{v}_k(t)$ using an optical setup.¹⁰⁹ The detailed procedure for obtaining information located at both diagonal and off-diagonal elements of $\hat{\rho}_k(t)$ from final $\mathbf{v}_k(t)$ is described in the supplementary information of Ref. 68.

C Simulation of the amplitude damping model with Kraus operators

We tested the theory mentioned in the previous section for spontaneous emission of a 2-level atom modeled by amplitude-channel damping. The corresponding Lindblad master equation is:

$$\dot{\hat{\rho}}(t) = \gamma \left[\sigma^+ \hat{\rho}(t) \sigma^- - \frac{1}{2} \{ \sigma^- \sigma^+, \hat{\rho}(t) \} \right],$$

where the spontaneous emission rate is $\gamma = 1.52 \times 10^9 \text{ s}^{-1}$, and the $\sigma^+ = |0\rangle\langle 1|$ and $\sigma^- = (\sigma^+)^\dagger$ are Pauli raising and lowering operators, respectively. The density matrix $\rho(t)$ in the Kraus representation is as follows:

$$\begin{aligned} \hat{\rho}(t) &= \mathcal{M}_0(t) \hat{\rho} \mathcal{M}_0(t)^\dagger + \mathcal{M}_1(t) \hat{\rho} \mathcal{M}_1(t)^\dagger, \\ \mathcal{M}_0(t) &= \frac{1+\sqrt{e^{-\gamma t}}}{2} \mathbf{I} + \frac{1-\sqrt{e^{-\gamma t}}}{2} \sigma_z = \begin{pmatrix} 1 & 0 \\ 0 & \sqrt{e^{-\gamma t}} \end{pmatrix}, \\ \mathcal{M}_1(t) &= \sqrt{1-e^{-\gamma t}} \sigma^+ = \begin{pmatrix} 0 & \sqrt{1-e^{-\gamma t}} \\ 0 & 0 \end{pmatrix}. \end{aligned} \tag{29}$$

For \mathcal{M}_k of dimension 2×2 , $\tilde{\mathcal{M}}_k$, $\tilde{\mathcal{N}}_k$, and \mathcal{D}_A are 4×4 matrices, as given below in Eq. (30). In this way, the 2-dilations $\mathcal{U}_{\mathcal{M}_k}$ and $\mathcal{U}_{\mathcal{N}_k}$ are 12×12 following the k -dilation.^{68,79} Note that, though these superoperators are time dependent, only for simplicity we omitted the notation of time dependency. However, realization of the dilated matrices using quantum gate is of dimension of form $2^n \times 2^n$. We append the dilated matrix with an ancillary 12×4 zero matrix on the right and 4×12 at the bottom, and an 4×4 identity matrix along the diagonal. The resulting dilated superoperator matrix is 16×16 , requiring 4 qubits for quantum implementation. Quantum implementation is accomplished with Qiskit as mentioned in the main text.

$$\begin{aligned}
\tilde{\mathcal{M}}_0 &= \begin{pmatrix} 1 & 0 & 0 & 0 \\ 0 & 1 & 0 & 0 \\ 0 & 0 & \sqrt{e^{-\gamma t}} & 0 \\ 0 & 0 & 0 & \sqrt{e^{-\gamma t}} \end{pmatrix}, & \tilde{\mathcal{N}}_0 &= \begin{pmatrix} 1 & 0 & 0 & 0 \\ 0 & \sqrt{e^{-\gamma t}} & 0 & 0 \\ 0 & 0 & 1 & 0 \\ 0 & 0 & 0 & \sqrt{e^{-\gamma t}} \end{pmatrix}, \\
\mathcal{D}_{\tilde{\mathcal{M}}_0} &= \begin{pmatrix} 0 & 0 & 0 & 0 \\ 0 & 0 & 0 & 0 \\ 0 & 0 & \sqrt{1-e^{-\gamma t}} & 0 \\ 0 & 0 & 0 & \sqrt{1-e^{-\gamma t}} \end{pmatrix}, & \mathcal{D}_{\tilde{\mathcal{N}}_0} &= \begin{pmatrix} 0 & 0 & 0 & 0 \\ 0 & \sqrt{1-e^{-\gamma t}} & 0 & 0 \\ 0 & 0 & 0 & 0 \\ 0 & 0 & 0 & \sqrt{1-e^{-\gamma t}} \end{pmatrix}. \\
\tilde{\mathcal{M}}_1 &= \begin{pmatrix} 0 & 0 & \sqrt{1-e^{-\gamma t}} & 0 \\ 0 & 0 & 0 & \sqrt{1-e^{-\gamma t}} \\ 0 & 0 & 0 & 0 \\ 0 & 0 & 0 & 0 \end{pmatrix}, & \tilde{\mathcal{N}}_1 &= \begin{pmatrix} 0 & \sqrt{1-e^{-\gamma t}} & 0 & 0 \\ 0 & 0 & 0 & 0 \\ 0 & 0 & 0 & \sqrt{1-e^{-\gamma t}} \\ 0 & 0 & 0 & 0 \end{pmatrix}, \\
\mathcal{D}_{\tilde{\mathcal{M}}_1} &= \begin{pmatrix} 1 & 0 & 0 & 0 \\ 0 & 1 & 0 & 0 \\ 0 & 0 & \sqrt{e^{-\gamma t}} & 0 \\ 0 & 0 & 0 & \sqrt{e^{-\gamma t}} \end{pmatrix}, & \mathcal{D}_{\tilde{\mathcal{N}}_1} &= \begin{pmatrix} 1 & 0 & 0 & 0 \\ 0 & \sqrt{e^{-\gamma t}} & 0 & 0 \\ 0 & 0 & 1 & 0 \\ 0 & 0 & 0 & \sqrt{e^{-\gamma t}} \end{pmatrix}.
\end{aligned} \tag{30}$$

For an initial density $\hat{\rho}(0) = \frac{1}{4} \begin{pmatrix} 1 & 1 \\ 1 & 3 \end{pmatrix}$, we calculate the populations in the basis $\{|0\rangle, |1\rangle\}$

from $t = 0$ to $t = 1000$ ps with a time step of 10 ps. With $\|\hat{\rho}\|_{HS} = \frac{\sqrt{3}}{2}$, the input state is:

$$\mathbf{v}_0 = \frac{1}{\|\hat{\rho}\|_{HS}} \left(\mathbf{v}_\rho^T, \overbrace{0, \dots, 0}^m \right)^T = \frac{1}{2\sqrt{3}} \left(1, 1, 1, 3, \overbrace{0, \dots, 0}^m \right)^T, \tag{31}$$

where $m = 12$ for the vector \mathbf{v}_ρ^T to be of length 16. After extracting the output $\mathbf{v}_k(t)$, the

ground state and excited state populations are obtained as the first and fourth entry of the vector, respectively. The Fig. 10 result manifests the consistency with the result in Ref. 68.

Acknowledgement

We acknowledge the financial support of the National Science Foundation under award number 2124511, CCI Phase I: NSF Center for Quantum Dynamics on Modular Quantum Devices (CQD-MQD). We acknowledge the use of IBM Quantum services for this work. The views expressed are those of the authors and do not reflect the official policy or position of IBM or the IBM Quantum team.

References

- (1) Wangsness, R. K.; Bloch, F. The dynamical theory of nuclear induction. *Phys. Rev.* **1953**, *89*, 728.
- (2) Redfield, A. G. On the theory of relaxation processes. *IBM Jr.* **1957**, *1*, 19.
- (3) Bloch, F. Generalized theory of relaxation. *Phys. Rev.* **1957**, *105*, 1206.
- (4) Haake, F. Statistical treatment of open systems by generalized master equations. *Springer Tracts Mod. Phys.* **1973**, *66*, 98.
- (5) Yoon, B.; Deutch, J. M.; Freed, J. H. A comparison of generalized cumulant and projection operator methods in spin-relaxation theory. *J. Chem. Phys.* **1975**, *62*, 4687–4696.
- (6) Lindblad, G. On the generators of quantum dynamical semigroups. *Commun. Math. Phys.* **1976**, *48*, 119.
- (7) Gorini, V.; Kossokowski, A.; Sudarshan, E. C. G. Completely positive dynamical semigroups of N-level systems. *J. Math. Phys.* **1976**, *17*, 821.

- (8) Oppenheim, I.; Shuler, K. E.; Weiss, G. H. *Stochastic Processes in Chemical Physics: The Master Equation*; MIT Press: Cambridge MA, 1977.
- (9) Alicki, R.; Lendi, K. *Quantum Dynamical Semigroups and Applications*; Springer-Verlag: Berlin, 1987.
- (10) Grabert, H. *Projection Operator Techniques in Nonequilibrium Statistical Mechanics*; Springer-Verlag: Berlin, 1982.
- (11) Kubo, R.; Toda, M.; Hashitsume, N. *Statistical Physics II - Nonequilibrium Statistical Mechanics*; Springer-Verlag: Berlin, 1983.
- (12) Laird, B. B.; Budimir, J.; Skinner, J. L. Quantum-mechanical derivation of the Bloch equations: Beyond the weak coupling limit. *J. Chem. Phys.* **1991**, *94*, 4391.
- (13) Kampen, N. G. V. *Stochastic Processes in Physics and Chemistry*; Elsevier: Amsterdam, 1992.
- (14) Pollard, W. T.; Felts, A. K.; Friesner, R. A. The Redfield equation in condensed-phase quantum dynamics. *Adv. Chem. Phys.* **1996**, *XCIII*, 77.
- (15) Kohen, D.; Marston, C. C.; J.Tannor, D. Phase space approach to theories of quantum dissipation. *J. Chem. Phys.* **1997**, *107*, 5236.
- (16) Kosloff, R.; Ratner, M. A.; Davis, W. B. Dynamics and relaxation in interacting systems: Semigroup approach. *J. Chem. Phys.* **1997**, *106*, 7036.
- (17) Cao, J. Phase space study of Bloch-Redfield theory. *J. Chem. Phys.* **1997**, *107*, 3204.
- (18) Shi, Q.; Geva, E. Stimulated Raman Adiabatic Passage in The Presence of Dephasing. *J. Chem. Phys.* **2003**, *119*, 11773–11787.

- (19) Baiz, C.; Kubarych, K.; Geva, E. Molecular theory and simulation of coherence transfer in metal carbonyls and its signature on multidimensional infrared spectra. *J. Phys. Chem. B* **2011**, *115*, 5322–5339.
- (20) Zwanzig, R. *Nonequilibrium Statistical Mechanics*; Oxford University Press: New York, 2001.
- (21) May, V.; Kühn, O. *Charge and Energy Transfer Dynamics in Molecular Systems*; Willey-VCH: Berlin, 2000.
- (22) Nitzan, A. *Chemical Dynamics in Condensed Phases*; Oxford University Press: New York, 2006.
- (23) Breuer, H.-P.; Petruccione, F. *The Theory of Open Quantum Systems*; Oxford Press: Oxford, 2002.
- (24) Jang, S. J. *DYNAMICS OF MOLECULAR EXCITONS*; Elsevier: Amsterdam, 2021.
- (25) Lai, Y.; Geva, E. On simulating the dynamics of electronic populations and coherences via quantum master equations based on treating off-diagonal electronic coupling terms as a small perturbation. *J. Chem. Phys.* **2021**, *155*, 204101–19.
- (26) Chen, H.; Lidar, D. A. Hamiltonian open quantum system toolkit. *Communications Physics* **2022**, *5*, 112.
- (27) Mulvihill, E.; Schubert, A.; Sun, X.; Dunietz, B. D.; Geva, E. A modified approach for simulating electronically nonadiabatic dynamics via the generalized quantum master equation. *J. Chem. Phys.* **2019**, *150*, 034101.
- (28) Mulvihill, E.; Lenn, K. M.; Gao, X.; Schubert, A.; Dunietz, B. D.; Geva, E. Simulating energy transfer dynamics in the Fenna-Matthews-Olson complex via the modified generalized quantum master equation. *J. Chem. Phys.* **2021**, *154*, 204109.

- (29) Mulvihill, E.; Geva, E. A Road Map to Various Pathways for Calculating the Memory Kernel of the Generalized Quantum Master Equation. *J. Phys. Chem. B* **2021**, *125*, 9834–9852.
- (30) Mulvihill, E.; Geva, E. Simulating the dynamics of electronic observables via reduced-dimensionality generalized quantum master equations. *J. Chem. Phys.* **2022**, *156*, 044119.
- (31) Xu, D.; Schulten, K. Coupling of protein motion to electron transfer in a photosynthetic reaction center: investigating the low temperature behavior in the framework of the spin–boson model. *Chem. Phys.* **1994**, *182*, 91–117.
- (32) Ishizaki, A.; Fleming, G. R. Quantum Coherence in Photosynthetic Light Harvesting. *Annu. Rev. Condens. Matter Phys.* **2012**, *3*, 333–361.
- (33) Liddell, P. A.; Kuciauskas, D.; Sumida, J. P.; Nash, B.; Nguyen, D.; Moore, A. L.; Moore, T. A.; Gust, D. Photoinduced charge separation and charge recombination to a triplet state in a carotene-porphyrin-fullerene triad. *J. Am. Chem. Soc.* **1997**, *119*, 1400–1405.
- (34) Liddell, P. A.; Kodis, G.; Moore, A. L.; Moore, T. A.; Gust, D. Photo switching of photoinduced electron transfer in a dithienylethene-porphyrin-fullerene triad molecule. *J. Am. Chem. Soc.* **2002**, *124*, 7668–7669.
- (35) Brédas, J.-L.; Beljonne, D.; Coropceanu, V.; Cornil, J. Charge-Transfer and Energy-Transfer Processes in π -Conjugated Oligomers and Polymers: A Molecular Picture. *Chem. Rev.* **2004**, *104*, 4971–5004.
- (36) Rizzi, A. C.; van Gastel, M.; Liddell, P. A.; Palacios, R. E.; Moore, G. F.; Kodis, G.; Moore, A. L.; Moore, T. A.; Gust, D.; Braslavsky, S. E. Entropic changes control the charge separation process in triads mimicking photosynthetic charge separation. *J. Phys. Chem. A* **2008**, *112*, 4215–4223.

- (37) Tian, H.; Yu, Z.; Hagfeldt, A.; Kloo, L.; Sun, L. Organic Redox Couples and Organic Counter Electrode for Efficient Organic Dye-Sensitized Solar Cells. *J. Am. Chem. Soc.* **2011**, *133*, 9413–9422.
- (38) Mishra, A.; Fischer, M. K. R.; Bäuerle, P. Metal-Free Organic Dyes for Dye-Sensitized Solar Cells: From Structure: Property Relationships to Design Rules. *Angew. Chem. Int. Ed.* **2009**, *48*, 2474–2499.
- (39) Feldt, S. M.; Gibson, E. A.; Gabrielsson, E.; Sun, L.; Boschloo, G.; Hagfeldt, A. Design of Organic Dyes and Cobalt Polypyridine Redox Mediators for High-Efficiency Dye-Sensitized Solar Cells. *J. Am. Chem. Soc.* **2010**, *132*, 16714–16724.
- (40) Zhao, Y.; Liang, W. Charge transfer in organic molecules for solar cells: Theoretical perspective. *Chem. Soc. Rev.* **2012**, *41*, 1075–1087.
- (41) Lee, M. H.; Dunietz, B. D.; Geva, E. Calculation From First Principles of Intramolecular Golden-Rule Rate Constants for Photo-Induced Electron Transfer in Molecular Donor-Acceptor Systems. *J. Phys. Chem. C* **2013**, *117*, 23391–23401.
- (42) Lee, M. H.; Dunietz, B. D.; Geva, E. Donor-to-Donor vs. Donor-to-Acceptor Interfacial Charge Transfer States in the Phthalocyanine-Fullerene Organic Photovoltaic System. *J. Phys. Chem. Lett.* **2014**, *5*, 3810–3816.
- (43) Hu, Z.; Engel, G. S.; Alharbi, F. H.; Kais, S. Dark states and delocalization: Competing effects of quantum coherence on the efficiency of light harvesting systems. *J. Chem. Phys.* **2018**, *148*, 064304.
- (44) Hu, Z.; Engel, G. S.; Kais, S. Double-excitation manifold's effect on exciton transfer dynamics and the efficiency of coherent light harvesting. *Phys. Chem. Chem. Phys.* **2018**, *20*, 30032–30040.

- (45) Daley, A. J. Quantum trajectories and open many-body quantum systems. *Adv. Phys.* **2014**, *63*, 77–149.
- (46) Wiseman, H. M.; Milburn, G. J. *Quantum Measurement and Control*; Cambridge University Press, 2009.
- (47) Brian, D.; Sun, X. Generalized quantum master equation: A tutorial review and recent advances. *Chin. J. Chem. Phys.* **2021**, *34*, 497–524.
- (48) Dan, X.; Xu, M.; Yan, Y.; Shi, Q. Generalized master equation for charge transport in a molecular junction: Exact memory kernels and their high order expansion. *J. Chem. Phys.* **2022**, *156*, 134114.
- (49) Kais, S. *Quantum Information and Computation for Chemistry*; John Wiley & Sons, Ltd, 2014; Chapter 1, pp 1–38.
- (50) Peruzzo, A.; McClean, J.; Shadbolt, P.; Yung, M.-H.; Zhou, X.-Q.; Love, P. J.; Aspuru-Guzik, A.; O’Brien, J. L. A variational eigenvalue solver on a photonic quantum processor. *Nat. Commun.* **2014**, *5*, 1–7.
- (51) O’Malley, P. J. J.; Babbush, R.; Kivlichan, I. D.; Romero, J.; McClean, J. R.; Barends, R.; Kelly, J.; Roushan, P.; Tranter, A.; Ding, N.; Campbell, B.; Chen, Y.; Chen, Z.; Chiaro, B.; Dunsworth, A.; Fowler, A. G.; Jeffrey, E.; Lucero, E.; Megrant, A.; Mutus, J. Y.; Neeley, M.; Neill, C.; Quintana, C.; Sank, D.; Vainsencher, A.; Wenner, J.; White, T. C.; Coveney, P. V.; Love, P. J.; Neven, H.; Aspuru-Guzik, A.; Martinis, J. M. Scalable quantum simulation of molecular energies. *Phys. Rev. X* **2016**, *6*, 031007.
- (52) Xia, R.; Bian, T.; Kais, S. Electronic structure calculations and the Ising Hamiltonian. *J. Phys. Chem. B* **2017**, *122*, 3384–3395.

- (53) Xia, R.; Kais, S. Quantum machine learning for electronic structure calculations. *Nat. Commun.* **2018**, *9*, 1–6.
- (54) Wiebe, N.; Berry, D. W.; Høyer, P.; Sanders, B. C. Simulating quantum dynamics on a quantum computer. *J. Phys. A Math. Theor.* **2011**, *44*, 445308.
- (55) Ollitrault, P. J.; Miessen, A.; Tavernelli, I. Molecular quantum dynamics: A quantum computing perspective. *Acc. Chem. Res.* **2021**, *54*, 4229–4238.
- (56) Yao, Y.-X.; Gomes, N.; Zhang, F.; Wang, C.-Z.; Ho, K.-M.; Iadecola, T.; Orth, P. P. Adaptive variational quantum dynamics simulations. *PRX Quantum* **2021**, *2*, 030307.
- (57) Tagliacozzo, L. Optimal simulation of quantum dynamics. *Nat. Phys.* **2022**, *18*, 970–971.
- (58) Lloyd, S.; Viola, L. Engineering quantum dynamics. *Phys. Rev. A* **2001**, *65*, 010101.
- (59) Wang, H.; Ashhab, S.; Nori, F. Quantum algorithm for simulating the dynamics of an open quantum system. *Phys. Rev. A* **2011**, *83*, 062317.
- (60) Wang, D.-S.; Berry, D. W.; De Oliveira, M. C.; Sanders, B. C. Solovay-kitaev decomposition strategy for single-qubit channels. *Phys. Rev. Lett.* **2013**, *111*, 130504.
- (61) Wei, S.-J.; Ruan, D.; Long, G.-L. Duality quantum algorithm efficiently simulates open quantum systems. *Sci. Rep.* **2016**, *6*, 1–9.
- (62) Kliesch, M.; Barthel, T.; Gogolin, C.; Kastoryano, M.; Eisert, J. Dissipative quantum church-turing theorem. *Phys. Rev. Lett.* **2011**, *107*, 120501.
- (63) Sweke, R.; Sinayskiy, I.; Bernard, D.; Petruccione, F. Universal simulation of Markovian open quantum systems. *Phys. Rev. A* **2015**, *91*, 062308.

- (64) Schlingens, A. W.; Head-Marsden, K.; Sager, L. M.; Narang, P.; Mazziotti, D. A. Quantum simulation of open quantum systems using a unitary decomposition of operators. *Phys. Rev. Lett.* **2021**, *127*, 270503.
- (65) Zhang, Y.; Hu, Z.; Wang, Y.; Kais, S. Quantum Simulation of the Radical Pair Dynamics of the Avian Compass. *The Journal of Physical Chemistry Letters* **2022**, *14*, 832–837.
- (66) Guimarães, J. D.; Lim, J.; Vasilevskiy, M. I.; Huelga, S. F.; Plenio, M. B. Noise-assisted digital quantum simulation of open systems. *arXiv preprint arXiv:2302.14592* **2023**,
- (67) Rossini, M.; Maile, D.; Ankerhold, J.; Donvil, B. I. Single Qubit Error Mitigation by Simulating Non-Markovian Dynamics. *arXiv preprint arXiv:2303.03268* **2023**,
- (68) Hu, Z.; Xia, R.; Kais, S. A quantum algorithm for evolving open quantum dynamics on quantum computing devices. *Sci. Rep.* **2020**, *10*, 1–9.
- (69) Head-Marsden, K.; Krastanov, S.; Mazziotti, D. A.; Narang, P. Capturing non-Markovian dynamics on near-term quantum computers. *Phys. Rev. Res* **2021**, *3*, 013182.
- (70) Hu, Z.; Head-Marsden, K.; Mazziotti, D. A.; Narang, P.; Kais, S. A general quantum algorithm for open quantum dynamics demonstrated with the Fenna-Matthews-Olson complex. *Quantum* **2022**, *6*, 726.
- (71) Nakajima, S. On the quantum theory of transport phenomena. *Prog. Theor. Phys.* **1958**, *20*, 948–959.
- (72) Zwanzig, R. Ensemble method in the theory of irreversibility. *J. Chem. Phys.* **1960**, *33*, 1338–1341.
- (73) Pfalzgraff, W.; Montoya-Castillo, A.; Kelly, A.; Markland, T. Efficient construction of

- generalized master equation memory kernels for multi-state systems from nonadiabatic quantum-classical dynamics. *J. Chem. Phys.* **2019**, *150*, 244109–16.
- (74) Fetherolf, J. H.; Berkelbach, T. C. Linear and nonlinear spectroscopy from quantum master equations. *J. Chem. Phys.* **2017**, *147*, 244109.
- (75) Fay, T. P.; Lindoy, L. P.; Manolopoulos, D. E. Electron spin relaxation in radical pairs: Beyond the Redfield approximation. *J. Chem. Phys.* **2019**, *151*, 154117.
- (76) Schile, A. J.; Limmer, D. T. Simulating conical intersection dynamics in the condensed phase with hybrid quantum master equations. *J. Chem. Phys.* **2019**, *151*, 014106.
- (77) Rivas, A.; Huelga, S. F. *Open quantum systems*; Springer, 2012; Vol. 10.
- (78) Lyu, N.; Mulvihill, E.; Soley, M. B.; Geva, E.; Batista, V. S. Tensor-Train Thermofield Memory Kernels for Generalized Quantum Master Equations. *Journal of Chemical Theory and Computation* **2023**, *19*, 1111–1129.
- (79) Levy, E.; Shalit, O. M. Dilation theory in finite dimensions: the possible, the impossible and the unknown. *Rocky Mt. J. Math.* **2014**, *44*, 203–221.
- (80) Gilyén, A.; Su, Y.; Low, G. H.; Wiebe, N. Quantum singular value transformation and beyond: exponential improvements for quantum matrix arithmetics. Proceedings of the 51st Annual ACM SIGACT Symposium on Theory of Computing. 2019; pp 193–204.
- (81) Camps, D.; Lin, L.; Van Beeumen, R.; Yang, C. Explicit Quantum Circuits for Block Encodings of Certain Sparse Matrices. *arXiv preprint arXiv:2203.10236* **2022**,
- (82) Nielsen, M. A.; Chuang, I. L. *Quantum Computation and Quantum Information: 10th Anniversary Edition*, 10th ed.; Cambridge University Press: New York, NY, USA, 2011.

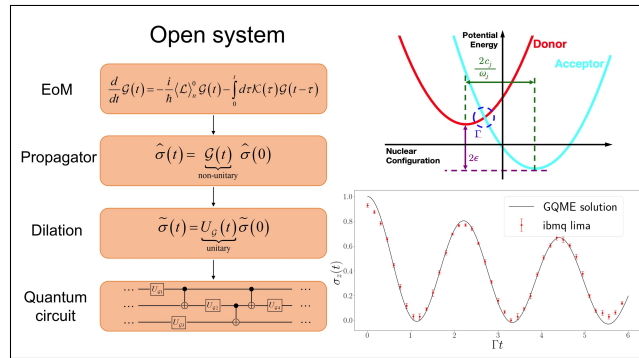
- (83) Reck, M.; Zeilinger, A.; Bernstein, H. J.; Bertani, P. Experimental realization of any discrete unitary operator. *Phys. Rev. Lett.* **1994**, *73*, 58–61.
- (84) Leggett, A. J.; Chakravarty, S.; Dorsey, A. T.; Fisher, M. P. A.; Garg, A.; Zwerger, W. Dynamics of the dissipative two-state system. *Rev. Mod. Phys.* **1987**, *59*, 1–85.
- (85) Weiss, U. *Quantum Dissipative Systems*, 4th ed.; WORLD SCIENTIFIC, 2012.
- (86) Shi, Q.; Geva, E. A new approach to calculating the memory kernel of the generalized quantum master equation for an arbitrary system-bath coupling. *J. Chem. Phys.* **2003**, *119*, 12063–12076.
- (87) Chatterjee, S.; Makri, N. Real-Time Path Integral Methods, Quantum Master Equations, and Classical vs Quantum Memory. *J. Phys. Chem. B* **2019**, *123*, 10470 – 10482.
- (88) Aleksandrowicz, G.; Alexander, T.; Barkoutsos, P.; Bello, L.; Ben-Haim, Y.; Bucher, D.; Cabrera-Hernández, F. J.; Carballo-Franquis, J.; Chen, A.; Chen, C.-F.; Chow, J. M.; Córcoles-Gonzales, A. D.; Cross, A. J.; Cross, A.; Cruz-Benito, J.; Cullver, C.; González, S. D. L. P.; Torre, E. D. L.; Ding, D.; Dumitrescu, E.; Duran, I.; Eendebak, P.; Everitt, M.; Sertage, I. F.; Frisch, A.; Fuhrer, A.; Gambetta, J.; Gago, B. G.; Gomez-Mosquera, J.; Greenberg, D.; Hamamura, I.; Havlicek, V.; Hellmers, J.; Łukasz Herok; Horii, H.; Hu, S.; Imamichi, T.; Itoko, T.; Javadi-Abhari, A.; Kanazawa, N.; Karazeev, A.; Krsulich, K.; Liu, P.; Luh, Y.; Maeng, Y.; Marques, M.; Martín-Fernández, F. J.; McClure, D. T.; McKay, D.; Meesala, S.; Mezzacapo, A.; Moll, N.; Rodríguez, D. M.; Nannicini, G.; Nation, P.; Ollitrault, P.; O’Riordan, L. J.; Paik, H.; Pérez, J.; Phan, A.; Pistoia, M.; Prutyanov, V.; Reuter, M.; Rice, J.; Davila, A. R.; Rudy, R. H. P.; Ryu, M.; Sathaye, N.; Schnabel, C.; Schoute, E.; Setia, K.; Shi, Y.; Silva, A.; Siraichi, Y.; Sivarajah, S.; Smolin, J. A.; Soeken, M.; Takahashi, H.; Tavernelli, I.; Taylor, C.; Taylour, P.; Trabing, K.; Treinish, M.; Turner, W.; Vogt-Lee, D.;

- Vuillot, C.; Wildstrom, J. A.; Wilson, J.; Winston, E.; Wood, C.; Wood, S.; Wörner, S.; Akhalwaya, I. Y.; Zoufal, C. Qiskit: An Open-source Framework for Quantum Computing. 2019; <https://doi.org/10.5281/zenodo.2562111>.
- (89) Vartiainen, J. J.; Möttönen, M.; Salomaa, M. M. Efficient decomposition of quantum gates. *Phys. Rev. Lett.* **2004**, *92*, 177902.
- (90) Gyongyosi, L. Quantum state optimization and computational pathway evaluation for gate-model quantum computers. *Sci. Rep.* **2020**, *10*, 1–12.
- (91) Lacroix, N.; Hellings, C.; Andersen, C. K.; Di Paolo, A.; Remm, A.; Lazar, S.; Krinner, S.; Norris, G. J.; Gabureac, M.; Heinsoo, J.; Blais, A.; Eichler, C.; Wallraff, A. Improving the performance of deep quantum optimization algorithms with continuous gate sets. *PRX Quantum* **2020**, *1*, 110304.
- (92) Iten, R.; Moyard, R.; Metger, T.; Sutter, D.; Woerner, S. Exact and practical pattern matching for quantum circuit optimization. *ACM Trans. Quantum Comput* **2022**, *3*, 1–41.
- (93) Abdessaied, N.; Wille, R.; Soeken, M.; Drechsler, R. Reducing the depth of quantum circuits using additional circuit lines. International Conference on Reversible Computation. 2013; pp 221–233.
- (94) Viola, L.; Lloyd, S. Dynamical suppression of decoherence in two-state quantum systems. *Phys. Rev. A* **1998**, *58*, 2733.
- (95) Uhrig, G. S. Keeping a quantum bit alive by optimized π -pulse sequences. *Phys. Rev. Lett.* **2007**, *98*, 100504.
- (96) Khodjasteh, K.; Lidar, D. A. Fault-tolerant quantum dynamical decoupling. *Phys. Rev. Lett.* **2005**, *95*, 180501.

- (97) Khodjasteh, K.; Lidar, D. A. Performance of deterministic dynamical decoupling schemes: Concatenated and periodic pulse sequences. *Phys. Rev. A* **2007**, *75*, 062310.
- (98) West, J. R.; Fong, B. H.; Lidar, D. A. Near-optimal dynamical decoupling of a qubit. *Phys. Rev. Lett.* **2010**, *104*, 130501.
- (99) Pokharel, B.; Anand, N.; Fortman, B.; Lidar, D. A. Demonstration of fidelity improvement using dynamical decoupling with superconducting qubits. *Phys. Rev. Lett.* **2018**, *121*, 220502.
- (100) Das, P.; Tannu, S.; Dangwal, S.; Qureshi, M. Adapt: Mitigating idling errors in qubits via adaptive dynamical decoupling. MICRO-54: 54th Annual IEEE/ACM International Symposium on Microarchitecture. 2021; pp 950–962.
- (101) Jurcevic, P.; Javadi-Abhari, A.; Bishop, L. S.; Lauer, I.; Bogorin, D. F.; Brink, M.; Capelluto, L.; Günlük, O.; Itoko, T.; Kanazawa, N.; Kandala, A.; Keefe, G. A.; Kruslich, K.; Landers, W.; Lewandowski, E. P.; McClure, D. T.; Nannicini, G.; Narasgond, A.; Nayfeh, H. M.; Pritchett, E.; Rothwell, M. B.; Srinivasan, S.; Sundaresan, N.; Wang, C.; Wei, K. X.; Wood, C. J.; Yau, J.-B.; Zhang, E. J.; Dial, O. E.; Chow, J. M.; Gambetta, J. M. Demonstration of quantum volume 64 on a superconducting quantum computing system. *Quantum Sci. Technol.* **2021**, *6*, 025020.
- (102) Ofek, N.; Petrenko, A.; Heeres, R.; Reinhold, P.; Leghtas, Z.; Vlastakis, B.; Liu, Y.; Frunzio, L.; Girvin, S.; Jiang, L.; Mirrahimi, M.; Devoret, M. H.; Schoelkopf, R. J. Extending the lifetime of a quantum bit with error correction in superconducting circuits. *Nature* **2016**, *536*, 441–445.
- (103) Hu, L.; Ma, Y.; Cai, W.; Mu, X.; Xu, Y.; Wang, W.; Wu, Y.; Wang, H.; Song, Y.; Zou, C.-L.; Girvin, S. M.; Duan, L.-M.; Sun, L. Quantum error correction and universal gate set operation on a binomial bosonic logical qubit. *Nat. Phys.* **2019**, *15*, 503–508.

- (104) Campagne-Ibarcq, P.; Eickbusch, A.; Touzard, S.; Zalys-Geller, E.; Frattini, N. E.; Sivak, V. V.; Reinhold, P.; Puri, S.; Shankar, S.; Schoelkopf, R. J.; Frunzio, L.; Mirrahimi, M.; Devoret, M. H. Quantum error correction of a qubit encoded in grid states of an oscillator. *Nature* **2020**, *584*, 368–372.
- (105) Paik, H.; Schuster, D. I.; Bishop, L. S.; Kirchmair, G.; Catelani, G.; Sears, A. P.; Johnson, B. R.; Reagor, M. J.; Frunzio, L.; Glazman, L. I.; Girvin, S. M.; Devoret, M. H.; Schoelkopf, R. J. Observation of high coherence in Josephson junction qubits measured in a three-dimensional circuit QED architecture. *Phys. Rev. Lett.* **2011**, *107*, 240501.
- (106) Reagor, M.; Pfaff, W.; Axline, C.; Heeres, R. W.; Ofek, N.; Sliwa, K.; Holland, E.; Wang, C.; Blumoff, J.; Chou, K.; Hatridge, M. J.; Frunzio, L.; Devoret, M. H.; Jiang, L.; Schoelkopf, R. J. Quantum memory with millisecond coherence in circuit QED. *Phys. Rev. B* **2016**, *94*, 014506.
- (107) Wang, C. S.; Curtis, J. C.; Lester, B. J.; Zhang, Y.; Gao, Y. Y.; Freeze, J.; Batista, V. S.; Vaccaro, P. H.; Chuang, I. L.; Frunzio, L.; Jiang, L.; Girvin, S. M.; Schoelkopf, R. J. Efficient multiphoton sampling of molecular vibronic spectra on a superconducting bosonic processor. *Phys. Rev. X* **2020**, *10*, 021060.
- (108) Wang, C. S.; Frattini, N. E.; Chapman, B. J.; Puri, S.; Girvin, S. M.; Devoret, M. H.; Schoelkopf, R. J. Observation of wave-packet branching through an engineered conical intersection. *Phys. Rev. X* **2023**, *13*, 011008.
- (109) Sparrow, C.; Martín-López, E.; Maraviglia, N.; Neville, A.; Harrold, C.; Carolan, J.; Joglekar, Y. N.; Hashimoto, T.; Matsuda, N.; O’Brien, J. L.; Tew, D. P.; Laing, A. Simulating the vibrational quantum dynamics of molecules using photonics. *Nature* **2018**, *557*, 660–667.

TOC Graphic



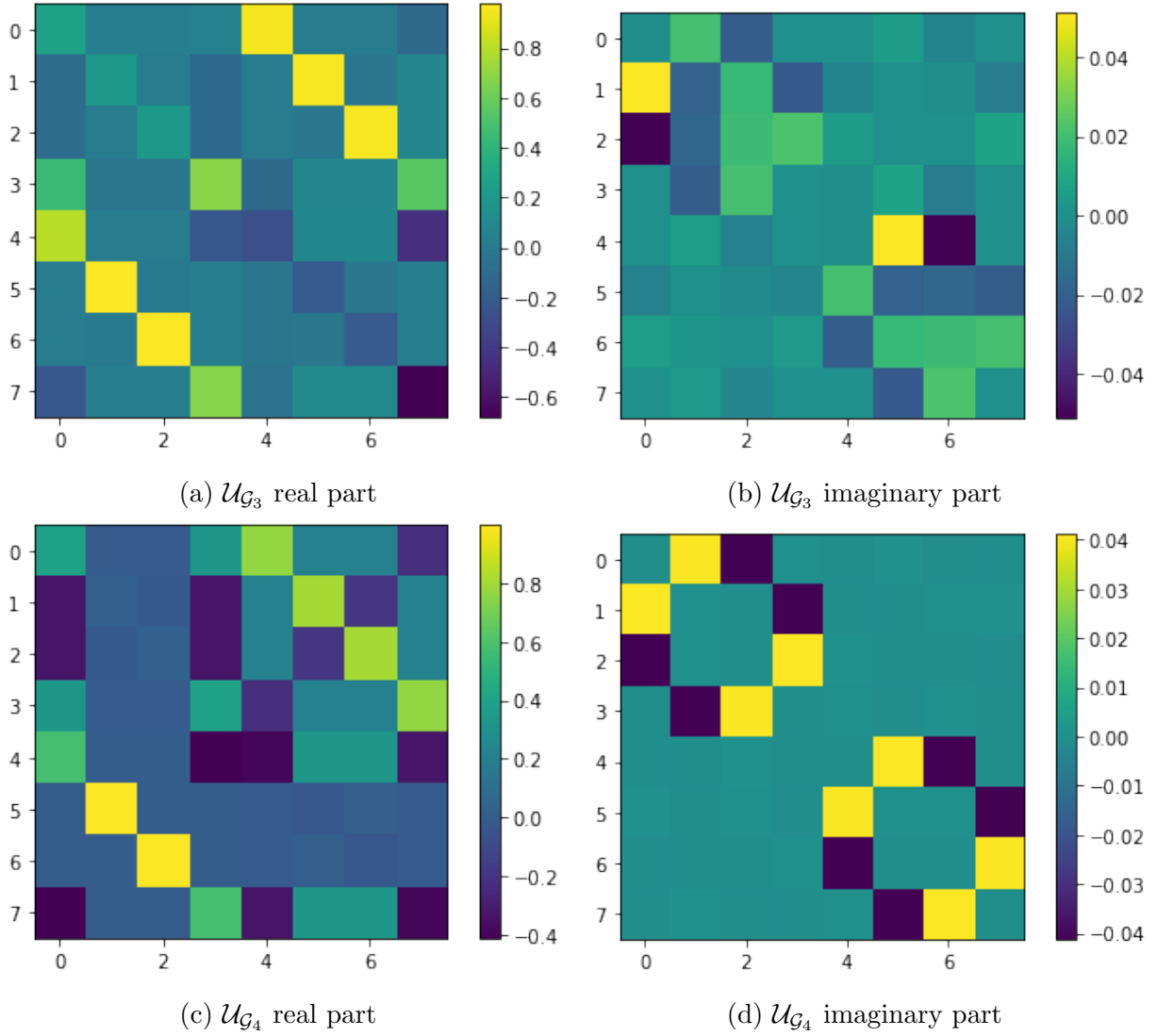
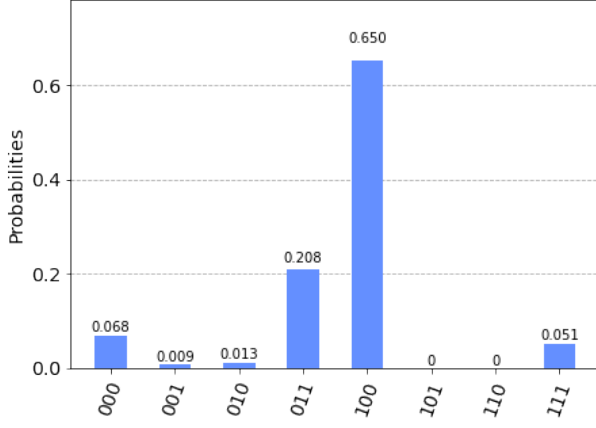
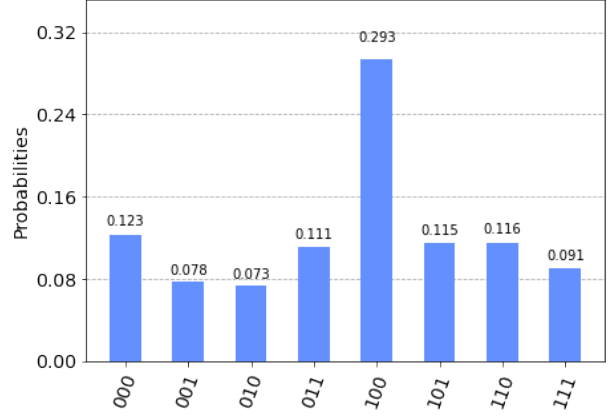


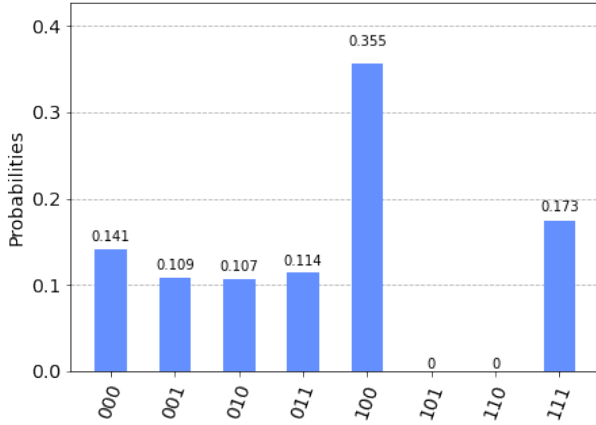
Figure 6: Heat map illustrations of the dilated 8×8 unitary matrix $\mathcal{U}_{\mathcal{G}_3}$ and $\mathcal{U}_{\mathcal{G}_4}$ for the 1500th $\mathcal{G}(t)$ matrix, \mathcal{G}_3 at $t = 2.25\Gamma^{-1}$ for model 3 with (a) the real part of the matrix and (b) the imaginary part of the matrix and \mathcal{G}_4 at $t = 6.75\Gamma^{-1}$ for model 4 with (c) the real part of the matrix and (d) the imaginary part of the matrix.



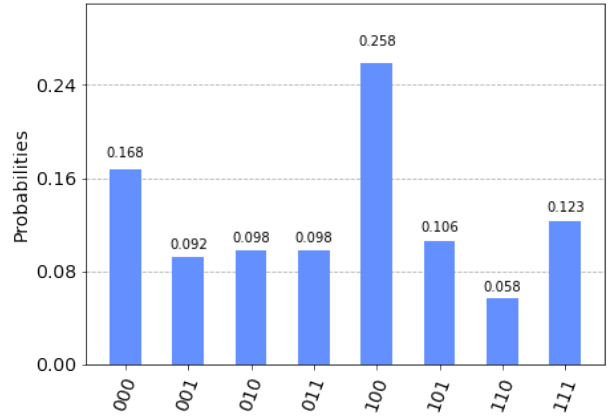
(a) QASM simulation of model 3



(b) **ibm quito** simulation of model 3



(c) QASM simulation of model 4



(d) **ibmq lima** simulation of model 3

Figure 7: Probability distribution of the quantum state after the projection measurement applied to the circuit for $\mathcal{U}_{\mathcal{G}_3}$ on (a) the QASM and (b) **ibm quito** quantum computer and $\mathcal{U}_{\mathcal{G}_4}$ on (c) the QASM and (d) **ibmq lima** quantum computer. The $|000\rangle$ state corresponds to the population squared of the donor state $\sigma_{DD}(t)$ and the $|100\rangle$ state corresponds to the population squared of the acceptor state $\sigma_{AA}(t)$. The last four states are ancilla states.

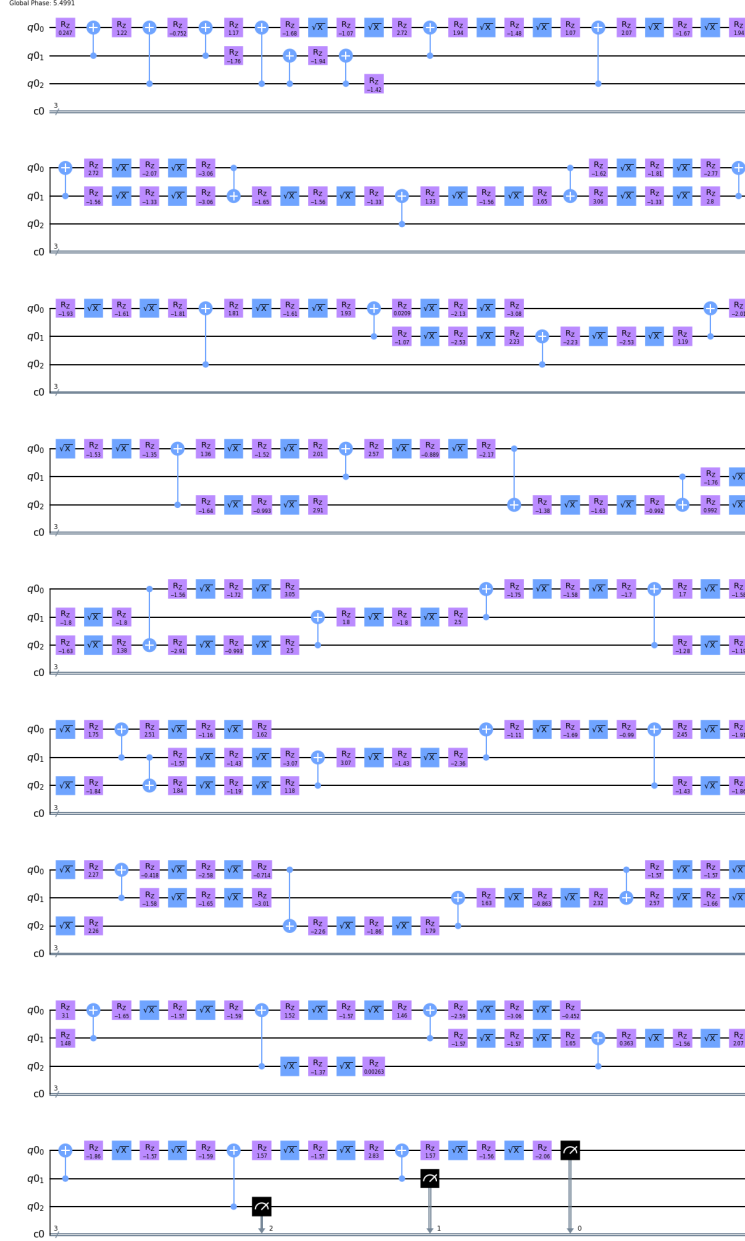


Figure 8: Transpiled quantum circuit of the dilated \mathcal{U}_{G_3} matrix at 1500 time steps for model 3. Each horizontal black line denotes a qubit. The \sqrt{X} gate (blue square) is the square root of X gate; the R_z gate (magenta square) is the rotation Z gate. The two-qubit gates are the controlled-NOT gate, where the dot denotes the controlled qubit and \oplus denotes the target qubit. The black gates at the end of the circuit denote the projection measurements. The number of required R_z , \sqrt{X} , and CNOT gates are 153, 98, and 41, respectively.

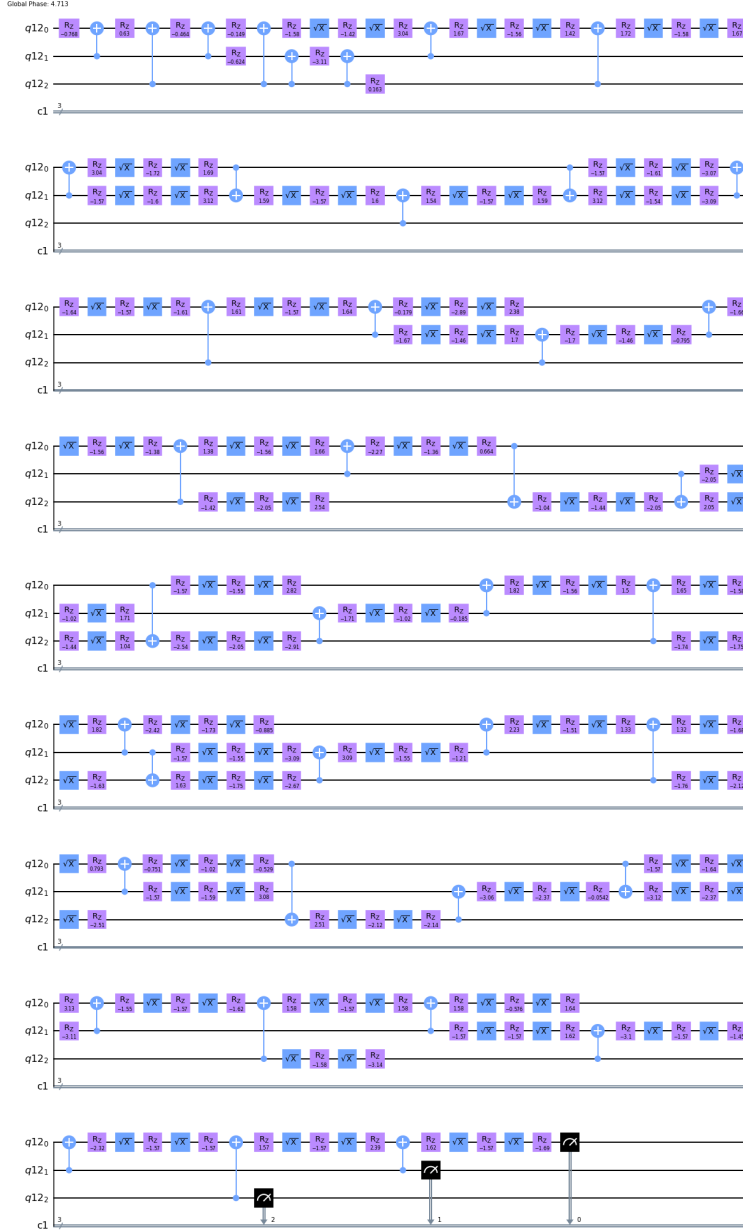


Figure 9: Transpiled quantum circuit of the dilated \mathcal{U}_{G_4} matrix at 1500 time steps for model 4. Each horizontal black line denotes a qubit. The \sqrt{X} gate (blue square) is the square root of X gate; the R_z gate (magenta square) is the rotation Z gate. The two-qubit gates are the controlled-NOT gate, where the dot denotes the controlled qubit and \oplus denotes the target qubit. The black gates at the end of the circuit denote the projection measurements. The number of required R_z , \sqrt{X} , and CNOT gates are 153, 98, and 41, respectively.

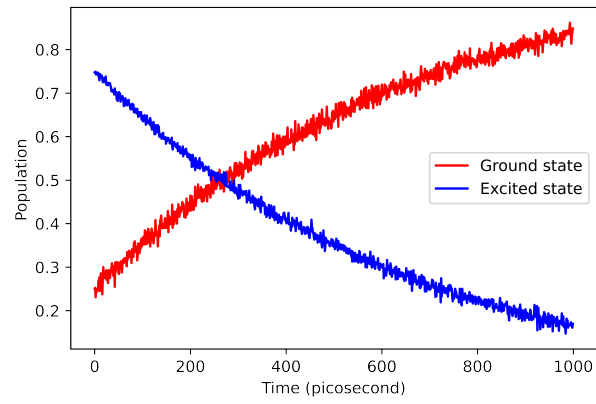


Figure 10: Population of ground state and excited state for the amplitude-damping model obtained by the quantum implementation on the IBM Qiskit simulator.